1-1-2012

# Role Of Compressibility And Slip In Blood Flow Through A Local Constriction

Tahmina Akhter
*Ryerson University*

# Role of Compressibility and Slip in Blood Flow through a local Constriction

by

Tahmina Akhter

Master of Philosophy, BUET, 2007

A thesis

presented to Ryerson University

in partial fulfillment of the

requirements for the degree of

Master of Science

in the Program of

Applied Mathematics

Toronto, Ontario, Canada, 2012

# Author's Declaration

I hereby declare that I am the sole author of this thesis. This is a true copy of the thesis, including any required final revisions, as accepted by my examiners.

I authorize Ryerson University to lend this thesis to other institutions or individuals for the purpose of scholarly research.

I further authorize Ryerson University to reproduce this thesis by photocopying or by other means, in total or in part, at the request of other institutions or individuals for the purpose of scholarly research.

I understand that my thesis may be made electronically available to the public.

# Abstract

Role of Compressibility and Slip in Blood Flow through a local Constriction

Master of Science 2012

Tahmina Akhter

Applied Mathematics

Ryerson University

One type of blood disease is a narrowing of a tubular structure, known as constriction or stenosis and high cholesterol is one of the main causes for this. Suitable mathematical models are important to describe this phenomenon, and to study the problem analytically and numerically. An approximate analytical solution and a recently developed particle-based method called multi-particle collision dynamics (MPC) is used to simulate the weakly compressible steady flow through a three-dimensional constricted axisymmetric cylinder. The particle collisions in *MPC* dynamics are numerically more efficient than other particle-based simulation methods. Particle interactions with the cylinder walls are modeled using slip as well as no-slip boundary conditions. Using an appropriate averaging procedure allows us to make a comparison between the approximate analytical solution and the numerical results. Significant and interesting differences were found in the velocity profiles obtained analytically and by using *MPC*.

# Acknowledgements

This is a great opportunity to show my gratitude to all those great people, who made this work possible. First of all I would like to thank my supervisor Dr. Katrin Rohlf for her tremendous support and patience to listen to me, to find out drawbacks of mine, and to give me valuable suggestions not only for the Thesis but also to make the decision for my future study. I also like to mention here that, despite of some maternal issues, she never stopped to give me her valuable time. I am also very grateful to the department of Mathematics at Ryerson, for providing me the best computational resources in the Ramlab. My department funded me a lot by giving me the maximum number of teaching assistantship hours. It is my great pleasure to have an IT specialist Steve Kanellis, who always solved my problems instantly and did his best to support me wherever he could. I am very thankful for my course teachers for their teaching, which gave me a very good foundation to do my research. Also the official staff of the department of Mathematics always did their best to complete my work. I am also thankful to my class-mates for their moral support and suggestions during the research. I will never forget, my junior friend George McBirnie, who worked in the Ramlab last summer, for his discussions and ideas about mathematics and programming. I am blessed by my parents and my in-laws all the time for their moral support from far away, during this work. There is no word to describe how much debt I have to my kids, who gave me the opportunity by not demanding me whenever they need, but just to have me as I could, which I think is the most excellent opportunity to make this work possible in a new country. I am also thankful to my family members, my brother Tawfiq, my sister Taslima, my cousin Tanjil and my brother-in-law Monir, for their caring support by providing me the valuable documents as necessary from my country. My former M Phil supervisor, Dr. Abdul Alim, is some-one so special for me to give me a platform in this mathematical arena and also continuing his moral support by giving the references as needed. My supervisory committee members Dr. Silvana Ilie and Dr. Jean-Paul Pascal have played an important role during this work. It is my blessing from God, to have someone as special as my life partner, Hasan Imam. Just because of him, I am who I am today. Finally I am thankful to OGS for funding this research work, to NSERC for the computational resources and to Ryerson University for giving me the opportunity to pursue a graduate degree in the Applied Mathematics program.

# Dedication

I would like to dedicate this Thesis to my mother, father and to my mother-in-law and father-in-law.

# Contents

# List of Tables

# List of Figures

# List of Appendices

# Chapter 1

# Introduction

Local constriction or *stenosis* is generally a term that describes the abnormal narrowing of an artery, although can also refer to a reduced cross-sectional area of a heart valve when it opens. In the case of an artery, stenosis most commonly occurs in the large distributing arteries such as the coronary artery, or in the large renal, cerebral, iliac or femoral arteries. A common cause of this narrowing is a chronic disease process called *atherosclerosis*. A focal vasospasm can also lead to acute vessel stenosis although in general, stenosis results from a vascular disease. If localized plaques develop within the wall of the artery, then the diameter of the artery is significantly reduced. Normal blood flow is thus disturbed, and can result in an atherosclerosic lesion in severe cases. Although the main causes of atherosclerotic lesions are still unknown, fluid dynamics parameters play a very important role as has already been established by many researchers. In addition to potential lesions, vessel occlusion is also of concern. The pressure distribution, the boundary layer separation, and the high and low arterial wall stresses have a major role in plaque formation in the artery [24]. Generally flow speeds up through the constriction and slows down when it has passed through it. This kind of sudden increase of flow speed rises the adverse pressure gradients for which low shear regions can occur near the wall of the vessel, possibly leading to recirculating zones. These recirculating regions can form upstream [18] or downstream [21] and depend on flow parameters, as well as on the stenosis geometry. Blood cells, such as platelets, trapped in low shear regions can stick together (aggregate) and adhere to the vessel wall, forming clots or thrombi, which we will refer to as aggregates to be general. If the aggregates form in recirculating regions upstream, then these aggregates could potentially lead to vessel blockage if they break off and

have become too large to pass through the constriction. Thus, it is important to be able to address flow through a constriction from a theoretical or numerical standpoint and to be able to propose treatment options based on analytical or *in silico* results.

Several researchers have studied the dynamics of blood flow through constrictions analytically [26] and numerically [24, 34, 39, 37]. Except for Misra and Shit [26] and Bedkihal [2], most works have been done using no-slip boundary conditions where the fluid velocity is set to zero at the solid boundary. The possibility of slip for blood was originally suggested by Nubar [30]. Hershey and Cho [13] studied blood flow experimentally in a rigid tube and also suggest that slip for blood is a reasonable assumption. They found that, if flow rate increases, it increases the thickness of the plasma film. Also, the effective slip velocity of the plasma film was found to increase monotonically with the flow rate, and this increase is a linear function of shear stress at high flow rates. Nakano *et. al* [27] investigated the velocity profile of blood flow in rat mesenteric arterioles by particle image velocimetry. They recorded the images of red blood cells in their experiments and they found slip near the vascular wall in their time averaged cross-section velocity profiles. Picart *et.al* [33] have also reported slip at the wall in their viscometric measurements of blood. These experimental findings indicate that one should perhaps consider wall slip in the study of blood flow, as the flow through the stenosis would be higher with slip at the wall compared to no-slip flow. If slip at the wall can be increased by injecting drugs [6], then even in the presence of stenosis, one could recover a proper flow rate of blood with incorporation of slip in one's studies. Also, with slip, the wall shear stress would be higher than in the no-slip case, so one could minimize the risk of formation of plaques by injecting drugs. Hence, we incorporate slip in our flow model for blood.

Compressibility too is often not incorporated in blood flow studies. With the recent birth of the use of particle-based methods for blood [5, 2, 43], where compressibility effects are built-in in the model, one has to be able to quantify the effect of compressibility in such models. Comparison to a theoretical model with and without compressibility might allow for proper assessment of this effect, as particle-based methods do not allow for removal of compressibility effects and such effects may well become important in complex flow geometries such as in a stenosis.

Since blood is a particle-based system that may have compressibility built-in, and since there seems to be some evidence of slip at the wall based on experimental results, we consider the flow of a weakly compressible fluid with and without slip, both analytically and numerically in this Thesis. For the

analytical results we follow the works of Forrester and Young [10] who completed the analysis for a steady, incompressible fluid through a smooth stenosis, and we extend the results here to allow for weak compressibility effects as well as slip at the wall. For the numerical simulations we pick a numerically efficient particle-based method called Multi-particle Collision Dynamics (MPC for short), whose average flow properties have been shown to agree with the Navier-Stokes Equations.

The basis of our analytical calculations comes from Forrester's Ph.D. Thesis in 1968 [9], where he investigated the flow through a converging-diverging tube and showed its implications in occlusive vascular disease. In 1970, Forrester and Young published the classical theoretical paper [10] in addition to some experimental results [11]. They used water and blood for their experiments, and used Reynolds numbers up to 1000. Although their experimental results did not differ much for water and blood, they found good agreement between the experimental and the theoretical results. Later Padmanabhan and Devanathan [32] extended the mathematical model to be able to predict the effects of turbulence in the stenosis. Their results indicate the existence of back-flow regions, and they provide cross-sections to demonstrate the effects.

The particle-based method, MPC, that was used in this Thesis has been used in a number of applications. For example, to simulate two-dimensional fluid flow past a circular and square cylinder, Lamura and Gompper [20] used the MPC dynamics. Following this work, Allahyarov and Gompper simulated three-dimensional flow past a sphere by MPC dynamics [1]. Flow around a fish-like shape using MPC dynamics has been simulated by Reid *et. el* [35]. Recently a model of a microswimmer has also been simulated using MPC dynamics [7]. Finally, MPC flow through a stenosis with slip and no-slip was recently considered in [2], although only one slip value was considered, the flow geometry was symmetric, and no analytical results were provided. Particle-based methods applied to flow through a constriction include [43, 5] and [2], the latter of which used MPC as we have done in this Thesis. The MPC method used in this Thesis was originally developed by Malevanets and Kapral [22]. The key advantage with this method is that it is possible to consider large particle systems in realistic computational times, as the idealized collision step conserves mass, momentum and energy, and the average flow properties (or *coarse-grained behaviour* of the system) has been shown to agree with the Navier-Stokes equations of motion [22]. Comprehensive reviews of the method can be found in [19, 12]. Several improvements of the method, which have also been incorporated here, include a grid-shifting mechanism introduced in [16], which ensures that there are no particle correlations due to particles that may reside in a collision

cell for more than one time step. Angular-conserving versions of MPC have been introduced in [28], which may be important in some applications, although not used here. A generalized particle-based boundary condition introduced in [4, 41] was implemented in the MPC dynamics, which allows us to vary the amount of slip at the wall exhibited by the coarse-grained behaviour of our system. To create flow in our stenosis, we introduce a force in the flow directions that acts on each particle at every time step. Since this adds energy to the system, and since we wish to achieve isothermal flow conditions, we use a velocity profile unbiased Galilean invariant thermostat [8, 31] which restores isothermal flow. For obtaining a coarse-grained description of our particle-based system we use a cumulative averaging method that was first introduced for MPC flow in [2], and has been used elsewhere as well [23, 22, 20].

In order to make comparisons between our analytical and numerical results, we pick a geometry that can be used in both analyses, and we extend the ideas in [25] to suit our needs. In particular, we pick a smooth polynomial form for the geometry using the ideas [25] and create an asymmetric stenosis geometry.

This Thesis is organized as follows: In Chapter 2 we provide the Fluid Dynamics background that is required for our analytical results. Chapter 3 provides an overview of the particle-based method (MPC) that was used for our numerical simulations. The details of our analytical calculations are presented in Chapter 4. Chapter 5 provides the results of our numerical simulations, and compares them to the analytical approximation derived in Chapter 4. Finally, Chapter 5 provides important conclusions and future work.

# Chapter 2

# Fluid Dynamics

## 2.1 Background

Fluid mechanics is the study of fluid either in motion (fluid dynamics) or at rest (fluid statics). From the fluid mechanics point of view, all matter consists of only two states, fluid and solid. A solid can resist a shear stress by a static deflection. On the other hand a fluid cannot resist a shear stress even if it is very small and as a result it starts to move and deform continuously until the effect of shear stress vanishes. There are two types of fluid, one is liquid and the other one is gas. A liquid has relatively closely packed molecules with strong cohesive forces, tends to retain its volume, and will form a free surface in a gravitational field if unconfined from above. On the other hand, a gas has no definite volume, and when left to itself without confinement, a gas forms an atmosphere that is essentially hydrostatic. Gases and liquids are both known as fluids and there are enormous Engineering and Applied science applications making this subject a contributing research area [40].

## 2.2 Navier-Stokes Equation

In order to talk about the dynamics of fluid, we need to derive the equations that govern the motion of a fluid. Basically there are two ways of derivation: the first treats a fluid as consisting of molecules whose motion is governed by the dynamic laws. From the molecular motion the macroscopic behavior of the

fluid is derived using the laws of mechanics and probability theory. The transport coefficients such as *coefficient of viscosity* and the *thermal conductivity* also come from the molecular concept. The theory is well developed for light gases, but it is incomplete for polyatomic gas molecules and for liquids. This way is discussed further in Chapter 3.

The alternative method used to derive the governing equations of motion, discussed in this chapter is the continuum method where individual molecules are ignored and the fluid is assumed to consist of continuous matter. In this continuous matter it is assumed that at each point there is a unique value of the field variables such as velocity, pressure, density etc. The continuous matter is then required to obey the conservation laws of mass, momentum, and energy which lead to the governing differential equations for the field variables. The variation of the field variables in space and time will then be defined by the solution of these differential equations, which corresponds to the mean value of the molecular magnitude of that field variable at each corresponding position and time. The statistical method treats gas flows in situations where the continuum concept is no longer valid. However the theory is incomplete for dense gases and for liquids.

Historically, fluid mechanics has been considered as part of the more general field of continuum mechanics, which deals with a relationship between forces, motions, and static conditions in continuous materials. Fluid mechanics deals with the study of all fluids under static and dynamic situations. This study area deals with many and diversified problems such as surface tension, fluid statics, flow in enclosed bodies, or flow around bodies (solid or otherwise), flow stability, etc. In fact, almost any action a person does involve some kind of a fluid mechanics problem.

A typical fluid system consists of the billions of atoms or molecules making up the fluid. To keep track of each molecule or atom is very difficult as fluid motion is a collective phenomenon. Fluid, in the continuum approach, can be thought of as made up of small volumes called *fluid elements* or *fluid particles* which themselves contain many atoms or molecules. The state of the fluid is determined by the density $\rho(\mathbf{r}, t)$, the velocity vector $\mathbf{v}(\mathbf{r}, t)$ and the pressure $p(\mathbf{r}, t)$, where $\mathbf{r} = (x, y, z)$ are the spatial coordinates and $t$ is the time. Please note that throughout the Thesis, bold-faced quantities denote vectors. The fundamental equations of motion in compressible viscous fluid dynamics are the Navier-Stokes equations (2.1)-(2.2).

The equation (2.3) is the continuity equation in the compressible case:

$$\rho\left(\frac{\partial \mathbf{v}}{\partial t} + \mathbf{v}\cdot\nabla\mathbf{v}\right) = -\nabla p + \nabla\cdot\tau + \mathbf{F} \quad \text{(conservation of momentum)}, \tag{2.1}$$

$$\tau = \mu\left(\nabla\mathbf{v} + \nabla\mathbf{v}^T - \frac{2}{3}\nabla\mathbf{v}\right) \quad \text{(constitutive equation)}, \tag{2.2}$$

$$\frac{\partial \rho}{\partial t} + \nabla\cdot\left(\rho\mathbf{v}\right) = 0 \quad \text{(conservation of mass)}. \tag{2.3}$$

Equation (2.2) is also called the shear stress constitutive equation. Here $\tau$ is the deviatoric stress tensor, $\mathbf{F}$ represents the body forces (per unit volume) acting on the fluid and $\mu$ is the *dynamic viscosity* of a given fluid and is a measure of resistance. The CGS unit of dynamic viscosity are "Poise" and the MKS unit is $Pa\cdot s$. Poise is defined as 1P=1g. In (2.1) the first term in the bracket is the usual acceleration term, and the second term represents convective acceleration making the entire equation non-linear. The convective acceleration is caused by the change in velocity over position. The first term on the right-hand side is the pressure gradient, in the second term $\tau$ is the deviatoric stress tensor which is defined by equation (2.2). Equations (2.1) - (2.3), represent a system of four differential equations with four unknowns ($\mathbf{v}$ and $p$) and can be solved numerically if we have appropriate boundary conditions. There are very few situations where equations (2.1)-(2.3) can be solved analytically.

## 2.3 Dynamic Similarity

Viscous fluid flows can be a complex study ranging from laminar to turbulent flows. The principle of *dynamic similarity* and *dimensional analysis* can be used to construct the solutions of Navier-Stokes equations. Generally, in fluid dynamics, one deals with flows through different geometries, or the flow past different geometrical objects, that introduces a characteristic linear dimension that is often the radius $R$ of the tube, or that of an object. *Kinematic viscosity*, which is defined by $\nu = \frac{\mu}{\rho}$, is another important quantity in fluid dynamics. This kinematic viscosity is measured in $m^2/s$ which are the units of a diffusion coefficient and that's why it is also known as *momentum diffusivity*. Now if we consider a stationary flow with velocity scale $U$ then from the concept of dimensional analysis it is possible to derive a dimensionless number which is known as the *Reynolds number* and can be defined as:

$$Re = \frac{RU}{\nu}. \tag{2.4}$$

The Reynolds number is a ratio of inertial to viscous forces. Using the dimensionless quantities $\frac{\mathbf{r}}{R}$ and $\frac{\mathbf{v}}{U}$ the solution of the steady, time independent Navier-Stokes equations can be written in the following form:

$$\frac{\mathbf{v}}{U} = \mathbf{f}\left(\frac{\mathbf{r}}{R}, Re\right). \tag{2.5}$$

This relation is true for every flow with the same Reynolds number. These types of flows are known as *dynamically similar flows*, and by rescaling, it is possible to get the respective solution in a simplified form. Equation (2.5) shows that the solution of the Navier-Stokes equations only depends on the dimensionless number.

## 2.4 Cylindrical Navier-Stokes Equations

The Navier-Stokes equations (2.1)-(2.3) for a general fluid in *cylindrical coordinates*, whose velocity $\mathbf{v} = (v_r, v_\theta, v_y) = (v(r,\theta,y,t), w(r,\theta,y,t), u(r,\theta,y,t))$ is given by

$$\text{continuity equation}: \frac{\partial \rho}{\partial t} + \frac{\partial(\rho u)}{\partial y} + \frac{1}{r}\frac{\partial(\rho r v)}{\partial r} + \frac{1}{r}\frac{\partial(\rho w)}{\partial \theta} = 0 \tag{2.6}$$

$$\begin{aligned} r-\text{momentum}: \quad & \rho\left(\frac{\partial v}{\partial t} + v\frac{\partial v}{\partial r} + \frac{w}{r}\frac{\partial v}{\partial \theta} - \frac{w^2}{r} + u\frac{\partial v}{\partial y}\right) \\ & = -\frac{\partial p}{\partial r} - \left(\frac{1}{r}\frac{\partial(r\tau_{rr})}{\partial r} + \frac{1}{r}\frac{\partial \tau_{r\theta}}{\partial \theta} - \frac{\tau_{\theta\theta}}{r} + \frac{\partial \tau_{ry}}{\partial y}\right) + F_r \end{aligned} \tag{2.7}$$

$$\begin{aligned} \theta-\text{momentum}: \quad & \rho\left(\frac{\partial w}{\partial t} + v\frac{\partial w}{\partial r} + \frac{w}{r}\frac{\partial w}{\partial \theta} - \frac{vw}{r} + u\frac{\partial w}{\partial y}\right) \\ & = -\frac{\partial p}{\partial \theta} - \left(\frac{1}{r^2}\frac{\partial(r^2\tau_{r\theta})}{\partial r} + \frac{1}{r}\frac{\partial \tau_{\theta\theta}}{\partial \theta} + \frac{\partial \tau_{\theta y}}{\partial y}\right) + F_\theta \end{aligned} \tag{2.8}$$

$$\begin{aligned} y-\text{momentum}: \quad & \rho\left(\frac{\partial u}{\partial t} + v\frac{\partial u}{\partial r} + \frac{w}{r}\frac{\partial u}{\partial \theta} + u\frac{\partial u}{\partial y}\right) \\ & = -\frac{\partial p}{\partial y} - \left(\frac{1}{r}\frac{\partial(r\tau_{ry})}{\partial r} + \frac{1}{r}\frac{\partial \tau_{\theta y}}{\partial \theta} + \frac{\partial \tau_{yy}}{\partial y}\right) + F_y \end{aligned} \tag{2.9}$$

The shear stress constitutive equation gives:

$$
\begin{aligned}
\tau_{rr} &= -\mu\left(2\tfrac{\partial v}{\partial r} - \tfrac{2}{3}(\nabla\cdot\mathbf{u})\right)\\
\tau_{\theta\theta} &= -\mu\left(2\left(\tfrac{1}{r}\tfrac{\partial w}{\partial \theta} + \tfrac{v}{r}\right) - \tfrac{2}{3}(\nabla\cdot\mathbf{u})\right)\\
\tau_{yy} &= -\mu\left(2\tfrac{\partial u}{\partial y} - \tfrac{2}{3}(\nabla\cdot\mathbf{u})\right)\\
\tau_{r\theta} = \tau_{\theta r} &= -\mu\left(r\tfrac{\partial}{\partial r}(\tfrac{w}{r}) + \tfrac{1}{r}\tfrac{\partial v}{\partial \theta}\right)\\
\tau_{ry} = \tau_{yr} &= -\mu\left(\tfrac{\partial u}{\partial r} + \tfrac{\partial v}{\partial y}\right)\\
\tau_{\theta y} = \tau_{y\theta} &= -\mu\left(\tfrac{\partial w}{\partial y} + \tfrac{1}{r}\tfrac{\partial u}{\partial \theta}\right)\\
\nabla\cdot\mathbf{u} &= \tfrac{1}{r}\tfrac{\partial}{\partial r}(rv) + \tfrac{1}{r}\tfrac{\partial w}{\partial \theta} + \tfrac{\partial u}{\partial y}
\end{aligned}
\tag{2.10}
$$

A flow of fluid through a pipe of uniform cross section is known as Hagen-Poiseuille flow. The velocity profile of Hagen-Poiseuille flow, for cylindrical flow, can be derived by using the equations by considering the following assumptions:

- The flow is steady (no time dependence).
- The azimuthal components of the fluid velocity is zero ($w = 0$).
- Flow is axisymmetric and fully developed ($u = u(r, y)$).

An approximate analytical solution to these equations in the compressible case will be discussed in Chapter 4.

# Chapter 3

# Particle-Based Methods

Researchers are paying attention to try to understand all the complex flow systems, and having more sophisticated computers available now, they have a tremendous scope to investigate these phenomena numerically, that's why computer simulations have a very important role in this sector. This is a virtual laboratory by which we can establish new numerical results, as well as validate experimental data. Nowadays fields like biomolecular dynamics, both the equilibrium and the non-equilibrium transport phenomena, electronic structure calculations, computational fluid dynamics, virology, astrophysical process and many more are using computer simulations as an essential tool to give some new ideas in the relevant fields. As complex fluid dynamics possesses many phenomena which are not well understood yet, computer simulations give a most authentic application to the system. Capturing the diverse spacial and temporal scales is the most challenging task when using the simulations.

Another example of a complex flow system is the multi-scale hierarchy in the circulatory system of blood. A typical micro particle diffuses over the length of its diameter in one second but displaces the billions of solvent molecules in a few picoseconds, in colloidal suspensions. Blood shows various behavior for various diameters of the vessel. Blood can be treated as a continuum in larger arteries, but in capillaries, where the diameter is of the size of a red blood cell, for the dominating effects of the particles, the continuum approximation is no longer appropriate.

In the study of biological systems, one of the main technical problems is the time-scale and length-scale gap between experimental and computational methods. In living system on an atomic level, the basis of all phenomena is formed by the chemical and mechanical processes. For understanding how

life works, experimental non-invasive methods of such dynamic processes would be greatly beneficial, however, generally experimental techniques do not achieve a resolution better than $ms - \mu s$ in time. On the other hand, there exist theoretical and computational methods, in particular molecular modeling, that enable the description of biological systems with all-atom detail. However up to now these approaches have been practically limited to simulation times and system sizes less than 100 $ns$ and 10 $nm$, respectively. A possible way to extend molecular modeling and to bridge it with experimental techniques is to use coarse-graining: to represent a system by a reduced (in comparison with an all-atom description) number of degrees of freedom. Due to the reduction in the degrees of freedom and elimination of fine interaction details, the simulation of a coarse-grained (CG) system requires less resources and goes faster than that for the same system in an all-atom representation. As a result, an increase of orders of magnitude in the simulated time and length scales can be achieved.

For complex flow phenomena, nowadays, there is a wide variety of discrete particle-based simulations available. They can be grouped into two main categories: one is *lattice-based* and the other one is *off-lattice* methods. There are two popular *lattice-based* simulation methods: one of them is the lattice Boltzmann method and the other one is lattice gas automata. Point-like particles, in these methods, stay on a regular lattice and move from node to node undergoing collisions when their trajectories meet. These collisions follow some simple collision rules. Correct hydrodynamic behavior can be obtained at macroscopic scales if these collision rules obey symmetry and invariance principles. It is easy to implement these methods and they are also computationally inexpensive. The dynamics of lattice-based methods are constrained by the configuration of the lattice which is the major drawback of these methods [23].

The *off-lattice* particle-based methods consider some other dynamics like dissipative particle dynamics (DPD), direct simulation Monte-Carlo methods (DSMC), and multiparticle collision dynamics (MPC) which is also known as Stochastic rotation dynamics (SRD). Originally Hoogerbrugge and Koelman introduced the dissipative particle dynamics in 1992 [14], which is a combination of molecular dynamics and Langevin dynamics. The time evolution of the system is described by Newton's equation of motion and it accommodates a set of particles with continuous positions and velocities. DPD is different from molecular dynamics due to the force term. The force acting on a particle has three parts, each of which is a sum of pair forces. The name of these forces are: conservative force, dissipative force and random force. In traditional DPD, the conservative force is considered to be soft repulsive, for which it is possible

to use a large time step and to rapidly achieve equilibrium. The dissipative force is the friction force which acts on the relative velocities of the particles. The loss of kinetic energy for dissipative forces is made up by the random forces. Both random and dissipative forces together ensure that the collisions of particles is an isothermal process.

The direct simulation Monte-Carlo (DSMC) method was proposed by Bird [3]. To solve the nonlinear time-dependent Boltzmann equations, the DSMC algorithm, which is a stochastic particle-based method can be used. The state of the system is given by the positions and velocities of the particles, in this DSMC simulation method. As in DPD, positions and velocities of the particles here are continuous variables. The geometry is divided into small cubical volumes, known as collision cells, which coarse-grains the system. Free-streaming and collisions are the two steps of the algorithm. In the free-streaming step particles move in such a way that they don't have any interaction with each other and their positions are updated using their velocities. Particles are selected randomly within the collision cell for collisions, in the collision step. According to kinetic theory, the collision probability for hard spheres is directly proportional to their relative velocity. If the particles $i$ and $j$ are selected as candidates for the collision, they are accepted as collision partners if $|\mathbf{v}_i - \mathbf{v}_j| > Rv_r^{max}$ where $v_r^{max}$ is the local maximum relative speed and $R$ is a random number chosen uniformly on the interval $[0, 1)$. To determine the collision probability, only the magnitude of the relative velocities of the particles are considered and for that reason, particles that are moving away from each other also collide. Imposing conservation of momentum and energy provides four of six equations to determine post collision velocities. The remaining two conditions are selected randomly, assuming that the direction of the post collision relative velocity is uniformly distributed on the unit sphere.

Multi-particle collision dynamics (MPC) has been used in this Thesis which was originally developed by Malevanets and Kapral [22]. This method has many of the features of DSMC described above. The most important difference between DSMC and MPC is the collision step. In the MPC collision step, the pre-collision velocity vector $\mathbf{v}_i'$ of a particle $i$ in collision cell $\xi$ is rotated by a randomly chosen rotation operator $\hat{\omega}_\xi$ relative to the average cell velocity $\mathbf{V}_\xi'$ to give the post-collision velocity

$$\mathbf{v}_i'' = \mathbf{V}_\xi' + \hat{\omega}_\xi(\mathbf{v}_i' - \mathbf{V}_\xi'), \tag{3.1}$$

where $\hat{\omega}$ is a stochastic rotation matrix that rotates the velocities by $+\alpha$ or $-\alpha$ and varies both in time

and from cell to cell. This type of collision is much more numerically efficient than the collision step of DSMC.

MPC has been used in a number of applications, for example to simulate two-dimensional fluid flow past a circular and square cylinder, Lamura and Gompper [20] used the MPC dynamics. Following this work, Allahyarov and Gompper simulated three-dimensional flow past a sphere by MPC dynamics [1]. Flow around a fish-like shape using MPC dynamics has been simulated by Reid *et. el* [35]. Recently a model of microswimmer has also been simulated by using MPC dynamics [7]. Very recent [2] simulated incompressible flow through a local constriction, using MPC dynamics. All these simulation results have been found to be in good agreement with empirical data and Navier-Stokes equations.

## 3.1 MPC dynamics

In this Thesis we use the *MPC* algorithm which consists of a numerically efficient mass, momentum and energy-conserving collision rule [23, 22] followed by acceleration, thermostatting and free-streaming. The collision cells are those of a regular lattice, and the system contains $N$ identical point particles of unit mass $m$ uniformly distributed on the lattice. In the $x$, $y$ and $z$ directions there are $L_x$, $L_y$ and $L_z$ cells respectively, and on average each cell $\xi$ contains $n$ particles. The velocities $\mathbf{v}_i$ and the continuous positions $\mathbf{r}_i$ of the particles *(i=1,2,....N)* are updated at discrete time intervals $\Delta t$. The momenta together with the particle positions form a phase space which is denoted by $\Gamma = (\mathbf{r}_i^N, \mathbf{p}_i^N) = (\mathbf{r}_1, m\mathbf{v}_1, ....., \mathbf{r}_N, m\mathbf{v}_N)$. For each of the $N$ particles in the system there are three momentum and position coordinates and so the dimension of the phase space is $6N$.

### 3.1.1 Multi-particle collision

The collision rule changes the pre-collision vector $\mathbf{v}_i'$ of particle $i$ by rotating it by a randomly selected rotation operator $\hat{\omega}_\xi$ relative to the average cell velocity (or center of mass velocity) $\mathbf{V}_\xi'$ to give the post-collision velocity

$$\mathbf{v}_i'' = \mathbf{V}_\xi' + \hat{\omega}_\xi(\mathbf{v}_i' - \mathbf{V}_\xi'), \tag{3.2}$$

where $\hat{\omega}$ is a stochastic rotation matrix that rotates the velocities by either $+\alpha$ or $-\alpha$ and varies both in time and from cell to cell. It is possible to show that momentum and energy are conserved by the above transformation. The proof is as follows: multiplying (3.2) by $m$ and summing over the number of particles $N_\xi$ in a given cell, and using the concept that the rotation operator is the same for all the particles in a given cell, gives:

$$\sum_{i=1}^{N_\xi} m\mathbf{v}_i'' = \sum_{i=1}^{N_\xi} m\Big(\mathbf{V}_\xi' + \hat{\omega}_\xi(\mathbf{v}_i' - \mathbf{V}_\xi')\Big) = \sum_{i=1}^{N_\xi} m\mathbf{v}_i' \tag{3.3}$$

$$\sum_{i=1}^{N_\xi} \frac{m}{2}|\mathbf{v}_i''|^2 = \sum_{i=1}^{N_\xi} \frac{m}{2}|\mathbf{V}_\xi' + \hat{\omega}_\xi(\mathbf{v}_i' - \mathbf{V}_\xi')|^2 = \sum_{i=1}^{N_\xi} \frac{m}{2}|\mathbf{v}_i'|^2 \tag{3.4}$$

For two-particle collisions, Figure 3.1 is the diagrammatic representation which demonstrates the rule in two dimensions, although the rule is applicable for any number of particles in a given collision cell and in any dimension. Note that, for clarity in the digram, the $\xi$ subscript has been dropped. MPC collisions are not pairwise collisions like DSMC and so MPC is much more numerically efficient.

### 3.1.2 Acceleration Flow and Thermostatting

In this Thesis, the flow in the *MPC* simulations is along the $y$-direction. A constant force $\mathbf{F} = m\mathbf{g} = (F_x, F_y, F_z) = (0, mg, 0)$ is applied to all the fluid particles to create flow and periodic boundary conditions have been applied in the $y$-direction. The post-collision velocities are updated according to

$$\mathbf{v}_i''' = \mathbf{v}_i'' + \frac{\mathbf{F}_i}{m}\Delta t. \tag{3.5}$$

If an external force is applied to the system in this way, energy is pumped into the system and henceforth the actual temperature, $T'$, of the system increases. The system has to be coupled to a thermostat, for isothermal flow at temperature $T$. To achieve isothermal flow conditions, a velocity profile unbiased Galilean invariant thermostat [8, 31] has been used in this work. The thermostat relates the instantaneous local temperature in a cell to the mean square deviation of the particle velocities computed from the

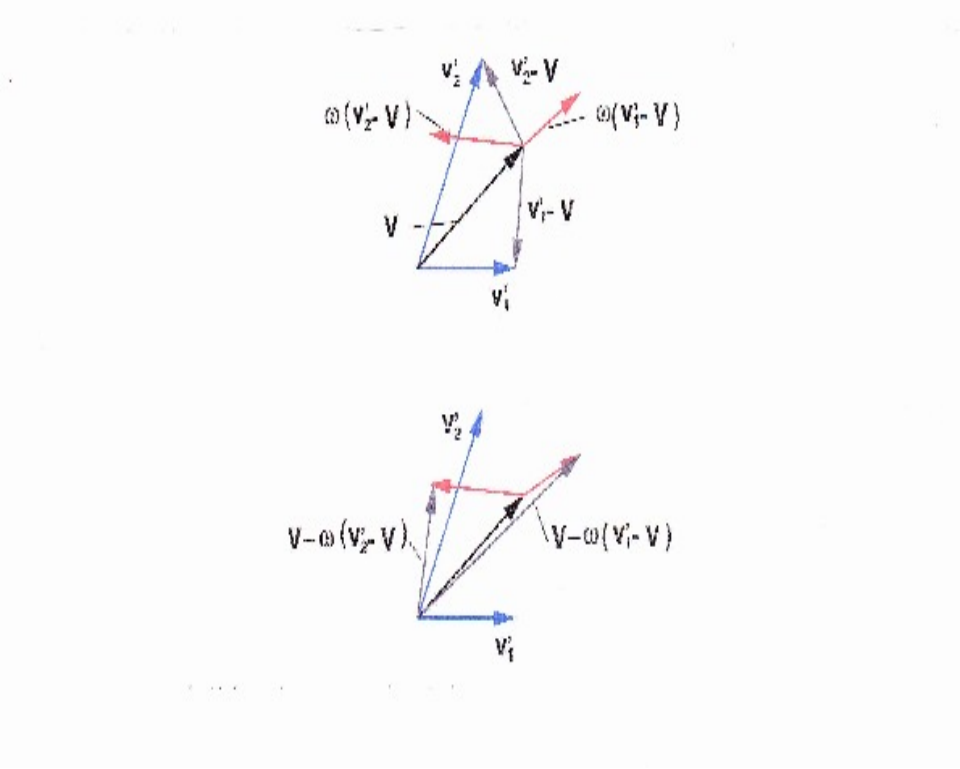


Figure 3.1: Diagramatic representation of the multiparticle collision rule. The upper panel shows the center of mass velocity and the pre-collision velocities of two particles relative to the center of mass. The lower panel shows the result of adding back the center of mass velocities to get the post-collision velocities. The figure is adapted from Anatoly-Malevanents and Raymond Kapral [23]

center of mass velocity of the cell. Mathematically, thermostatting scales the velocities according to

$$k_B T' = \frac{m}{N_{free}} \sum_{\xi} \sum_{i \in \xi} \left( \mathbf{v}_i''' - \mathbf{V}_\xi''' \right)^2 \tag{3.6}$$

$$N_{free} = \sum_{\xi} \begin{cases} 3(N_\xi - 1)(N_\xi > 1) \\ 0 \qquad\quad (N_\xi \leq 1) \end{cases} \tag{3.7}$$

$$\mathbf{v}_i = \mathbf{V}_\xi''' + \sqrt{\frac{T}{T'}} (\mathbf{v}_i''' - \mathbf{V}_\xi''') \tag{3.8}$$

In equations (3.6) and (3.7), recall that $N_\xi$ is the number of particles in the cell $\xi$. Note that the local temperature is undefined in cells of one or two particles. The thermostat acts by rescaling the relative velocities $\left( \mathbf{v_i}''' - \mathbf{V}_\xi''' \right)$ by $\sqrt{\frac{T}{T'}}$ at each time step according to equation (3.8).

### 3.1.3 Free-streaming, Liouville and *H*-Theorems

The positions of the particles are updated by free-streaming according to

$$\mathbf{r}_i = \mathbf{r}_i' + \mathbf{v}_i \Delta t \tag{3.9}$$

where $\mathbf{r}_i'$ is the position of the particle $i$ at the beginning of the time step and $\mathbf{v}_i$ is the velocity after collision, acceleration and thermostatting have taken place. It is possible to verify that the transformation corresponding to free-streaming is canonical, that is, it has unit Jacobian determinant.

Like the *Liouville* theorem, the collision and the free-streaming preserves the phase space volume, which is possible to show. At time $t$ and $t+\Delta t$ let the phase point of the system be $(\mathbf{r}_i'^N, \mathbf{v}_i'^N)$ and $(\mathbf{r}_i^N, \mathbf{v}_i^N)$. At time $t+\Delta t$ the phase space volume can be written as,

$$d\mathbf{x}^N = d\mathbf{r}^N d\mathbf{v}^N \tag{3.10}$$

Now let $p(\hat{\omega}|\mathbf{v}'^N)$ be the conditional probability of rotation given the velocity $\mathbf{v}'^N$. Using this equation (3.10), can be written as

$$d\mathbf{x}^N = d\mathbf{r}^N \sum_{\mathbf{v}'^N} p(\hat{\omega}|\mathbf{v}'^N) d\mathbf{v}'^N = d\mathbf{x}'^N \sum_{\mathbf{v}'^N} p(\hat{\omega}|\mathbf{v}'^N) = d\mathbf{x}'^N \tag{3.11}$$

where $d\mathbf{r}^N = d\mathbf{r}'^N$ and $\sum_{\mathbf{v}'^N} = 1$, by using the fact that velocities do not depend on the rotations. The Boltzmann $H$-functional has the form

$$H = \int d\mathbf{v} d\mathbf{r} f(\mathbf{v}, \mathbf{r}, t) \ln f(\mathbf{v}, \mathbf{r}, t), \tag{3.12}$$

where $f(\mathbf{v}, \mathbf{r}, t)$ is the reduced single particle distribution function. In time the $H$-functional decreases [23] and the minimum equilibrium value is the Maxwell-Boltzmann distribution

$$f(\mathbf{v}, \mathbf{r}, t) = \frac{N}{V} \left( \frac{m}{2\pi k_B T} \right)^{d/2} e^{-m\|\mathbf{v}-\mathbf{V}\|^2/2k_B T}, \tag{3.13}$$

where $V$ is the system volume, $\mathbf{V}$ is the average velocity of particles, $N$ is the average number of particles in the system, $k_B$ is the Boltzmann constant and $T$ is the system temperature. We like to mention here that, as a result of non-monotomic decay, numerical instabilities exhibited in other popular particle-based methods, such as lattice Boltzmann and lattice gas methods are not presented in *MPC*. By invoking a Chapman-Enskog expansion [22], it is possible to derive the hydrodynamic equations from the reduced probability distribution. After averaging the second-order terms in the Chapman-Enskog expansion one obtains the familiar Navier-Stokes equations.

### 3.1.4 Boundary Conditions

The presence of interfaces have a strong effect on the dynamics of the fluid flow. For the fluid in contact with a solid face, on the macroscopic scale, the normal component of the velocity at the interface must be zero. This represents an impassable boundary. The tangential velocity depends on the molecular interactions at the interface. *No-slip* (stick) and *slip* boundary conditions are two ideal situations. The tangential velocity of the fluid relative to that of the boundary vanishing is known as the no-slip condition, but with slip, the tangential velocity of the fluid is non-zero.

At the mesoscopic level there are several ways to implement these two boundary conditions. A generalized boundary condition has been used in this work, which includes *Bounce-back* (BB) and *loss in tangential and reversal of normal* (LIT). Malevanents and Kapral [23, 22] first proposed the *BB* boundary condition for the *MPC* dynamics. This boundary condition corresponds to the no-slip boundary conditions and is often used in lattice Boltzmann simulations [43]. The normal and the tangential com-

ponent of velocities of the particles are reversed in *BB* after the particle collides with the wall. For this situation the average relative velocity of the fluid near the wall vanishes (macroscopic no-slip) because the relative velocity distribution of particles reflected from the wall mirrors the distribution of particles approaching the wall [41]. This is similar to a frictional wall or perfectly rough wall. Meanwhile the tangential velocity component of the particles is lost for the case of *LIT*, for which the average velocity of the fluid near the wall is non-zero which leads to (macroscopic) slip. This type of wall is called a rough wall. For the endothelium and other layers there are porous in nature, we can consider blood vessels as not very smooth, so a small slip might be present at the wall. Considering the definition of rough walls, one can consider the vessel wall as rough. In more general mathematical form, the boundary conditions of the particle-based simulations is

$$\mathbf{v}_n = -\mathbf{v}'_n, \tag{3.14}$$

$$\mathbf{v}_t = \big(2\lambda - 1\big)\mathbf{v}'_t. \tag{3.15}$$

To indicate as normal and tangential, the subscripts $n$ and $t$ have been used and $\mathbf{v}$, $\mathbf{v}'$ indicate the post and pre-collision velocities of a particular particle hitting the wall. From the above equation it can be seen that $\lambda = 0$ corresponds to *BB*, and $\lambda = 0.5$ correspond to *LIT*. By changing the values of $\lambda$, we can vary the slip. The uniform flow can be obtained for perfect slip, that is, for $\lambda = 1$. Note that $\lambda \in (0, 1)$, gives rise to is a dissipative boundary condition that does not conserve energy. Since we are implementing a thermostat in our simulations, this is not an issue.

### 3.1.5 Grid shifting

There is a possibility of collisions for the same particles more than once with each other if the mean free path is less than the cell size, that is, if the temperature of the system and henceforth the average distance between subsequent collisions is small. Also near the boundary of the flow domain is a place where multiple collisions are possible. This can lead to the breakdown of Galilean invariance, violating the molecular chaos assumption. The grid shifting mechanism proposed by Ihle and Kroll [16, 17] can solve the problem and for that reason this mechanism has been used in this work. In this grid shifting mechanism, all particles are shifted by the same uniformly distributed random translation vector before the collision step takes place. In this way, the positions of the particles are randomized by the shift and Galilean invariance is restored.

## 3.2 Averaging Procedure

The computation of mean fluid velocity is very easy in particle-based methods but there can be bias in the measurement, which has been explained by Tysanner and Garcia [38]. Sample average measurement (SAM) and cumulative average measurement (CAM) are the two commonly used averaging methods. The SAM capture the average particle velocity in each cell at each sample, and then averages these over all the samples. The CAM sums the velocities of all particles in a cell over the samples, and then divides this cumulative sum by the cumulative total number of particles in the cell to get the mean velocity per cell. SAM can have bias by virtue of the correlations of fluctuations in the system. CAM is used in this work to avoid these correlations. Mathematically CAM can be described as

$$\left\langle \mathbf{u}_\xi \right\rangle = \frac{\sum_{j=1}^{s} \sum_{i\in\xi}^{N_\xi(t_j)} \mathbf{v}_i(t_i)}{\sum_{j=1}^{s} N_\xi(t_j)} \tag{3.16}$$

In the above equation $\xi$ again refers to the cell number, $i \in \xi$ means that particle $i$ is inside cell number $\xi$ at time $t_j$, $N_\xi(t_j)$ is the number of particles in cell $\xi$ at time $t_j$ and $\left\langle \mathbf{u}_\xi \right\rangle$ is the macroscopic velocity vector for the particles in the same cell. Here $S$ represents the number of samples used in the averaging process. We have assumed ergodicity and used one very long simulation rather than using different samples for a fixed time interval. It is common to average from one simulation [23, 22, 20] under the ergodic assumption. It has been argued that the stochastic nature of *MPC* dynamics leads to noisy averages [31], but it is possible to have a smooth average by using the CAM method. There will be more examples based on the CAM method in the surface velocity plots and velocity profiles, shown in Chapter 5.

## 3.3 Transport Coefficients and Re

The most wonderful capacity of the MPC dynamics is that it is possible to estimate the analytic viscosity and other transport coefficients. The fluid viscosity $\mu$ consists of the sum of a kinetic component $\mu_{kin}$ and a collision part $\mu_{coll}$, which has been shown by Noguchi and Gompper [29]. The simple 3-d expressions,

for the $\alpha = \frac{\pi}{2}$ rule (rule used in this work), are given by

$$\mu_{kin} = \left(\frac{\rho k_B T}{m}\right)\Delta t\left[\frac{5n}{6\big(n-1+e^{-n}\big)} - \frac{1}{2}\right] \tag{3.17}$$

$$\mu_{coll} = \frac{m}{18a_0\Delta t}\big(n-1+e^{-n}\big) \tag{3.18}$$

$$\mu = \mu_{kin} + \mu_{coll} \tag{3.19}$$

where $\rho = mn/a_0^3$ is the mass density, $n$ is the average number of particles in a cell and $a_0$ is the length of the cell.

In gravity-driven flow, the constant force, in an unconstricted tube, corresponds to a pressure drop per unit length of $dp/dy = -\rho g$, where $dp/dy$ is the pressure gradient in our flow geometry. The system becomes stable when the gravitational force balances the shear force and the velocity profile corresponds to the well-known laminar Poiseuille flow namely,

$$v_y(r) = \frac{1}{4\mu}\frac{dp}{dy}(r^2 - R_0^2). \tag{3.20}$$

Here $v_y(r)$ is the non-vanishing component of the macroscopic flow velocity that depends only on the radial distance $r$ from the $y$-axis, $R_0$ is the radius of the cylinder, and $\mu$ is the dynamic viscosity which has been computed from equation (3.19). To be mentioned here is that the $y$-component of the average velocity of (3.16) should agree with that of (3.20), in the unconstricted portion of the geometry and also the $r$ and $\theta$ components of the velocity should vanish.

The centerline velocity $U_0$ can be evaluated from (3.20) and is ($r = 0$):

$$U_0 = -\frac{dp}{dy}\frac{R_0^2}{4\mu} = \frac{\rho g R_0^2}{4\mu} \tag{3.21}$$

Thus, the Reynolds number by using (2.4) becomes

$$Re = \frac{R_0\overline{U}}{\nu} = \frac{R_0 U_0}{2\nu}, \tag{3.22}$$

which can be changed by varying the value of $g$ (see (3.21)), as $\rho$, $R_0$ and $\mu$ are fixed in our simulations. Note that we have chosen the velocity scale $U$ in (2.4) to be the mean velocity, $\overline{U}$.

# Chapter 4

# Analytical results

## 4.1 Geometry

The flow geometry is shown in Figure 4.1. The radius of the cylinder, $R(y)$, is a function of the longitudinal coordinate system $y$, with cross section in the $xz$-plane. A polynomial form for the geometry is chosen based on ideas in [25]. The geometry in [25], was chosen for an overlapping stenosis that is symmetric about the center of the location of the maximum constriction. Following the concept, here we extend the idea to make an asymmetric ($l_1 \neq l_2$ in Fig.4.1) stenosis geometry that is axially symmetric.

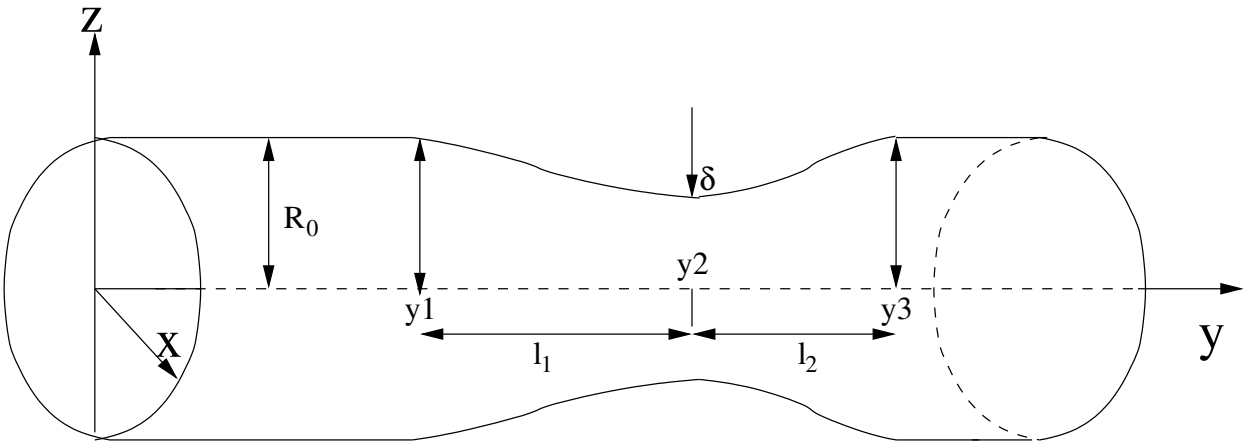


Fig.4.1: Flow Geometry.

In order to compare the analytical results with the particle-based method, a piecewise smooth (i.e. differentiable) geometry has been chosen which fixes some of the coefficients in $R(y)$, we pick the general form

$$R(y) = \begin{cases} R_0, \quad \text{for } y \leq y_1 \\ ay^3 + by^2 + cy + d \equiv A(y) \qquad \text{for } y_1 < y \leq y_2, \\ ey^3 + fy^2 + gy + h \equiv B(y) \qquad \text{for } y_2 < y \leq y_3, \\ R_0 \quad \text{for } y \geq y_3, \end{cases} \tag{4.1}$$

and impose conditions to get the unknowns ($a$ to $h$). For $R(y)$ to be continuous, we impose:

$$\begin{aligned} A(y_1) &= R_0 \\ A(y_2) &= B(y_2) \\ B(y_3) &= R_0 \end{aligned}$$

For $R(y)$ to be differentiable, we impose:

$$\begin{aligned} A'(y_1) &= 0 \\ A'(y_2) &= B'(y_2) \\ B'(y_3) &= 0 \end{aligned}$$

We also pick $y_2 = y_1 + l_1$ and $y_3 = y_2 + l_2$. In order for the maximum throat of constriction to be at $y_2$, we also impose:

$$\begin{aligned} A(y_2) &= R_0 - \delta \\ A'(y_2) &= 0 \end{aligned} \quad .$$

By implementing all those imposed conditions we evaluate the unknowns (from $a$ to $h$) and then get the radius $R(y)$ of the cylinder in the following idealized form:

$$R(y) = \begin{cases} R_0 \quad \text{for } y \leq y_1, \\ \frac{2\delta}{l_1^3}y^3 - \frac{3\delta(2y_1+l_1)}{l_1^3}y^2 + \frac{6\delta y_1(y_1+l_1)}{l_1^3}y - \frac{2\delta y_1^3+3\delta y_1^2 l_1 - R_0 l_1^3}{l_1^3} & \text{for } y_1 < y \leq y_2, \\ \frac{-2\delta}{l_2^3}y^3 + \frac{3(2y_1+2l_1+l_2)\delta}{l_2^3}y^2 - \frac{6\delta(y_1^2+2y_1 l_1+l_1^2+y_1 l_2+l_1 l_2)}{l_2^3}y & \\ + \frac{3\delta l_1^2 l_2+3\delta y_1^2 l_2+6\delta y_1 l_1 l_2+2\delta l_1^3+2\delta y_1^3+6\delta y_1^2 l_1+6\delta y_1 l_1^2+R_0 l_2^3-\delta l_2^3}{l_2^3} & \text{for } y_2 < y \leq y_3, \\ R_0 \quad \text{for } y \geq y_3, \end{cases} \tag{4.2}$$

where

$$x = R(y)cos\theta \tag{4.3}$$

$$y = R(y)sin\theta \tag{4.4}$$

The parameters in $R(y)$ have the following meaning (see Fig.4.1):

$R_0$ is the radius of the non-constricted portion of the cylinder,

$y_1$ is the location at the start of the constriction,

$y_2$ is the location of the maximum constriction,

$y_3$ is the location at the end of the constriction,

$l_1$ is the distance between the start $y_1$ and maximum constriction location $y_2$,

$l_1 + l_2$ is the length of the constriction,

and $\delta \geq 0$ controls the degree of constriction.

## 4.2 Approximate scaled velocity

We consider the flow of a compressible, steady (for which $\frac{\partial}{\partial t} = 0$) and axisymmetric (for which $w = 0$) fluid in cylindrical form. The governing equations from Chapter 2.4, now take the following form:

$$\rho\left(v\frac{\partial u}{\partial r} + u\frac{\partial u}{\partial y}\right)$$

$$= -\frac{\partial p}{\partial y} + \mu\left(\frac{4}{3}\frac{\partial^2 u}{\partial y^2} + \frac{\partial^2 u}{\partial r^2} + \frac{1}{3}\frac{\partial^2 v}{\partial y \partial r} + \frac{1}{3r}\frac{\partial v}{\partial y} + \frac{1}{r}\frac{\partial u}{\partial r}\right) + F_y, \tag{4.5}$$

$$\rho\left(v\frac{\partial v}{\partial r} + u\frac{\partial v}{\partial y}\right)$$

$$= -\frac{\partial p}{\partial r} + \mu\left(\frac{4}{3}\frac{\partial^2 v}{\partial r^2} + \frac{4}{3r}\frac{\partial v}{\partial r} - \frac{4}{3r^2}v + \frac{1}{3}\frac{\partial^2 u}{\partial y \partial r} + \frac{\partial^2 v}{\partial y^2}\right) + F_r, \tag{4.6}$$

where $u = u(r, y)$ and $v = v(r, y)$ are the velocity components in the $y$ and $r$ directions and $p$, $\rho$, $\mu$ are the pressure, density and viscosity of the fluid respectively. The continuity equation in this case takes the form:

$$\frac{1}{r}\frac{\partial(\rho r v)}{\partial r} + \frac{\partial(\rho u)}{\partial y} = 0 \tag{4.7}$$

Although there is no suitable means to obtain the exact solution for the equations (4.5)-(4.7) due to the nonlinear terms, it is possible to derive an approximate solution that can be useful to characterize the flow through the constriction [10].

To determine if any of the terms in equations (4.5) and (4.6) might be expected to have negligible effects in the problem being considered, an order-of-magnitude analysis was performed . The equations were written in terms of dimensionless space variables and velocity components, which had an order of magnitude of unity or less. If $\frac{\delta}{l_1}$ or $\frac{\delta}{l_2}$ is small compared to 1, then the axial normal stress gradient in equation (4.5) is negligible compared to the gradient of the shear component [9]. The radial variation in pressure can be neglected if $\delta/R_0$ is small. Thus for a mild stenosis. i.e. one for which $\frac{\delta}{l_1}$ or $\frac{\delta}{l_2}$ and $\frac{\delta}{R_0}$ are small, equations (4.5) and (4.6) can be approximated as:

$$v\frac{\partial u}{\partial r} + u\frac{\partial u}{\partial y} = -\frac{1}{\rho}\frac{\partial p}{\partial y} + \nu\left(\frac{4}{3}\frac{\partial^2 u}{\partial y^2} + \frac{\partial^2 u}{\partial r^2} + \frac{1}{r}\frac{\partial u}{\partial r} - \frac{1}{3}\frac{\partial}{\partial y}\left(\frac{1}{\rho}\frac{\partial}{\partial y}(\rho u)\right)\right) + g, \tag{4.8}$$

and

$$\frac{\partial p}{\partial r} = 0, \tag{4.9}$$

where the continuity equation was also used to replace $\frac{\partial v}{\partial y}$ in (4.5), $\nu = \frac{\mu}{\rho}$, and $\mathbf{F} = (F_r, F_\theta, F_y) = (0, 0, \rho g)$.

Making a Boussinesq-like approximation, where $\rho \approx \rho_0$=constant except in the pressure gradient term.

we can integrate (4.8) accross the cylinder. From (4.9) we see that $p = p(r, y) = p(y)$, so

$$\begin{aligned} \int_o^R r(-\tfrac{1}{\rho}\tfrac{\partial p}{\partial y})dr &= -\tfrac{1}{\rho_0}\tfrac{dp}{dy}(y)\int_0^R r dr \\ &= -\tfrac{1}{\rho_0}\tfrac{dp}{dy}\tfrac{R^2}{2}. \end{aligned}$$

Assuming flow in the radial direction is negligible compared to the flow in the $y$ direction, and that changes of flow in the $y$ direction depend on changes in $y$, more than changes in radius, we can say that $v\frac{\partial u}{\partial r} \ll u\frac{\partial u}{\partial y}$. Thus neglecting the term $v\frac{\partial u}{\partial r}$, equation (4.8) can be integrated across the cylinder to give (Appendix A):

$$\begin{aligned} \frac{1}{2}\frac{d}{dy}\int_0^R ru^2\, dr &= -\frac{1}{\rho}\frac{dp}{dy}\frac{R^2}{2} + g\frac{R^2}{2} + \nu R\Big(\frac{\partial u}{\partial r}\Big)_R + \nu\frac{d^2}{dy^2}\Big(\frac{\pi R^2\overline{U}}{2\pi}\Big) \\ &\quad -\frac{\nu}{3}\frac{\partial}{\partial y}\Big(\frac{1}{\rho}\frac{\partial \rho}{\partial y}\Big)\Big(\frac{\pi R^2\overline{U}}{2\pi}\Big). \end{aligned} \tag{4.10}$$

Here, $\overline{U}$ is the mean velocity at any given cross section of radius $R(y)$ and $Q$ is the volume rate of flow given by:

$$Q = \pi\rho R^2\overline{U} = \int_0^R 2\pi\rho ru\, dr. \tag{4.11}$$

Following [10], we now assume that the radial dependence of the axial velocity can be expressed as a fourth order polynomial of the form:

$$\frac{u}{U} = A\eta + B\eta^2 + C\eta^3 + D\eta^4 + E, \tag{4.12}$$

where $\eta = \frac{(R-r)}{R}$, $U$ is the centerline velocity, and we have to determine the coefficients from $A$ to $E$. This method is similar to the Karman-Pohlhausen method (Schlichting [36]), commonly used for laminar boundary layer study. This method has a very good application for various boundary layer problems and gives good results for accelerated flows but is not that reliable for retarded flows. However our problem is not the boundary layer problem.

The coefficients in equation (4.11) are evaluated using the following five boundary conditions:

(a) at $r = R$, $u = \frac{u_s}{\sqrt{1+R'(y)^2}}$, (normal component of velocity vanishes and the tangential component has magnitude $u_s$)

(b) at $r = 0$, $\frac{\partial u}{\partial r} = 0$, (axisymmetric flow)

(c) at $r = 0$, $u = U$, (by definition of U)
(d) at $r = R, \frac{dp}{dy} = \mu\left(\frac{\partial^2 u}{\partial r^2} + \frac{1}{r}\frac{\partial u}{\partial r}\right) + F_y$, (obtained from equation (4.8))
(e) at $r = 0$, $\frac{\partial^2 u}{\partial r^2} = -\frac{2U}{R^2}$, (nearly parabolic flow)

The boundary conditions for slip at the wall and axisymmetric flow are given by (a) and (b). Condition (c) is simply a definition, and (d) is obtained from equation (4.8). To obtain the condition (e), it is assumed that at $r = 0$ the velocity profile at the center of the tube is nearly parabolic ($u = U[1-(r/R)^2]$), so that at $r = 0$ the second derivative of $u$ can be approximated by (e). This last condition is from the assumption that only near the wall the velocity profile will significantly deviate from the parabolic form. Thus equation (4.12) becomes:

$$\begin{aligned}\frac{u}{U} &= \left(\frac{-\lambda + 10 - 12E + \tilde{T}}{7}\right)\eta + \left(\frac{3\lambda + 5 - 6E - 3\tilde{T}}{7}\right)\eta^2 \\ &\quad + \left(\frac{-3\lambda - 12 + 20E + 3\tilde{T}}{7}\right)\eta^3 + \left(\frac{\lambda + 4 - 9E - \tilde{T}}{7}\right)\eta^4 + E, \qquad (4.13)\end{aligned}$$

where $\lambda = \dfrac{dp}{dy}\dfrac{R^2}{\mu U}$,

$$\tilde{T} = \frac{gR^2}{\nu U}, \qquad (4.14)$$

and $E = \dfrac{u_s}{U\sqrt{1 + R'(y)^2}}$,

Now from the equation (4.13) we note that the velocity profile is a function of the single parameter $\lambda$ which depends on the value of the pressure gradient. Substituting equation (4.13) in equation (4.11) and then by integrating, the centerline velocity, $U$ can be expressed as (Appendix B)

$$U = \frac{210}{97\pi}\frac{Q}{\rho R^2} + \frac{2}{97}\frac{R^2}{\mu}\frac{dp}{dy} - \frac{2}{97}\frac{R^2\rho g}{\mu} - \frac{102}{97}\frac{u_s}{\sqrt{1 + R'(y)^2}}. \qquad (4.15)$$

The parameter $\lambda$ is determined from the momentum equation (4.8). The flow can be described as 'Poiseuille' flow through the stenosis if the non-linear term in (4.10) is neglected, [9]. In the present study, we did not neglect counting the non-linearity, but assumed that the velocity profile is nearly parabolic in the center for evaluating the integral, i.e.

$$u = 2\overline{U}\big[1 - (\frac{r}{R})^2\big], \qquad (4.16)$$

where $\overline{U}$ is the mean velocity at the given cross section. This type of approximation has been used by [15] in their study of unsteady flow through flexible tubes. This procedure is the combination of 'successive approximation' together with the momentum-integral technique [42], described that for mild stenosis and for low Reynolds numbers the velocity profile has parabolic distribution. Thus this assumption is valid for low Reynolds numbers.

Substituting equation (4.16) in the left hand side of equation (4.10) and evaluation of the integral reduces the momentum equation to (see equation (B.3) Appendix B.2):

$$\frac{d}{dy}\big(\frac{1}{3}\overline{U}^2R^2\big) = -\frac{1}{\rho}\frac{dp}{dy}\frac{R^2}{2} + \frac{1}{2}gR^2 + \nu R(\frac{\partial u}{\partial r})_R + \nu\frac{d^2}{dy^2}(\frac{\pi R^2\overline{U}}{2}) - \frac{\nu}{3}\frac{\partial}{\partial y}(\frac{1}{\rho}\frac{\partial\rho}{\partial y}(\frac{R^2\overline{U}}{2})) \tag{4.17}$$

Now expressions for $U$ and $(\frac{\partial u}{\partial r})_R$ from equations (4.15) and (4.13) are substituted in equation (4.17) to give an expression which, when combined with equation (4.14) yields for the pressure gradient (see Appendix B.2)

$$\frac{dp}{dy} = \frac{\frac{75}{194}gR^2 + \frac{2}{3\pi^2}\frac{Q^2}{\rho^2R^3}\frac{dR}{dy} - \frac{300\nu Q}{97\pi\rho R^2} + \frac{312}{97}\frac{\nu u_s}{\sqrt{1+R'^2(y)}}}{\left(\frac{75}{194}\frac{R^2}{\rho} - \frac{2}{3\pi^2}\frac{Q^2m}{\rho^3R^2k_BT}\right)}. \tag{4.18}$$

Equation (4.15) and equation (4.18) can be substituted in equation (4.13) to give the velocity $u$ as a function of $r$ and $y$ (see Appendix B.3):

$$\begin{aligned}
&\frac{u}{\overline{U}}\\
&= \frac{gR^2Ma^2}{\nu\overline{U}\big(1-\frac{388}{225}Ma^2\big)}\left(-\frac{44}{225}\eta + \frac{172}{225}\eta^2 - \frac{4}{5}\eta^3 + \frac{4}{5}\eta^4\right)\\
&+\frac{Re}{\big(1-\frac{388}{225}Ma^2\big)}\frac{dR}{dy}\left(-\frac{44}{225}\eta + \frac{172}{225}\eta^2 - \frac{4}{5}\eta^3 + \frac{4}{5}\eta^4\right)\\
&+\frac{1}{\big(1-\frac{388}{225}Ma^2\big)}\left(\big(4-\frac{16}{3}Ma^2\big)\eta + \big(-2-\frac{8}{3}Ma^2\big)\eta^2 + \frac{32}{5}Ma^2\eta^3 - \frac{32}{15}Ma^2\eta^4\right)\\
&+\frac{u_s}{\overline{U}\sqrt{1+R'^2(y)}\big(1-\frac{388}{225}Ma^2\big)}\left(-\frac{104}{25}\eta + \frac{52}{25}\eta^2 + \frac{4}{5}\eta^3 - \frac{3}{5}\eta^4 + 1 + \Big(\frac{416}{75}\eta + \frac{208}{75}\eta^2 - \frac{1808}{225}\eta^3 + \frac{244}{75}\eta^4 - \frac{388}{225}\Big)Ma^2\right).
\end{aligned} \tag{4.19}$$

Here $Ma = \frac{\overline{U}}{\sqrt{\frac{k_BT}{m}}}$ is the Mach number and $Re = \frac{\overline{U}R}{\nu}$ is the Reynolds number, where $k_B$ is the Boltzmann constant and $T$ is the system temperature. The scaled centerline velocity as a function of $r$

and $y$ at $\eta = 1$ ($r = 0$) is thus given by:

$$\begin{aligned}
\tfrac{u}{U_0} &= \tfrac{u}{2\overline{U}_0} \\
&= \tfrac{1}{2}\big(\tfrac{u}{\overline{U}}\big)\big(\tfrac{\overline{U}}{\overline{U}_0}\big) \\
&= \tfrac{(\frac{R_0}{R})^2(\frac{\rho_0}{\rho})}{2\big(1-\frac{388}{225}Ma^2\big)}\Bigg[\tfrac{8}{225}Ma^2\Big(\tfrac{R_0 g}{\overline{U}_0^2}\Big)Re_0\Big(\tfrac{R}{R_0}\Big)^4\Big(\tfrac{\rho}{\rho_0}\Big)\Big(\tfrac{\nu_0}{\nu}\Big) \\
&+ \tfrac{8}{225}Re_0\Big(\tfrac{\rho_0}{\rho}\Big)\Big(\tfrac{R_0}{R}\Big)\Big(\tfrac{\nu_0}{\nu}\Big)\tfrac{dR}{dy} + \Big(2 - \tfrac{56}{15}Ma^2\Big) \\
&+ \tfrac{u_s}{\sqrt{1+R'^2(y)}}\big(\tfrac{R}{R_0}\big)^2\tfrac{\rho}{\rho_0}\tfrac{1}{\overline{U}_0}\Big(-\tfrac{22}{25} + \tfrac{136}{75}Ma^2\Big)\Bigg],
\end{aligned} \tag{4.20}$$

where $Re_0$, $\rho_0$, $\overline{U}_0$ and $\nu_0$ are the Reynolds number, density, mean velocity and viscosity far upstream respectively. Note that we assume constant flow rate, that is

$$\begin{aligned}
Q \quad &= \quad \pi\rho R^2\overline{U}(y) = \pi\rho_0 R_0^2\overline{U}_0(y) \\
&\Longrightarrow \quad \tfrac{\overline{U}}{\overline{U}_0} = (\tfrac{\rho_0}{\rho})(\tfrac{R_0}{R})^2,
\end{aligned}$$

so that we can write the Reynolds number $Re = \frac{\overline{U}R}{\nu}$ (compare with (3.22)) in terms of the values far upstream. In other words,

$$\begin{aligned}
Re \quad &= \quad \tfrac{\overline{U}R}{\nu} \\
&= \quad Re_0\tfrac{\overline{U}}{\overline{U}_0}\tfrac{R}{R_0}\tfrac{\mu_0}{\mu}\tfrac{\rho}{\rho_0} \\
&= \quad Re_0(\tfrac{\rho_0}{\rho})(\tfrac{R_0}{R})(\tfrac{\nu_0}{\nu})
\end{aligned}$$

where $Re_0 = \frac{\overline{U}_0 R_0}{\nu_0}$ is the Reynolds number far upstream. For comparison with the numerical results in the next Chapter, we plot (4.19) and (4.20) using the values of $Re_0$, $Ma$ etc. based on the numerical simulations.

Note that a similar analysis leading to (4.19)-(4.20) was carried out by Forrester and Young [10] for incompressible, no-slip flow and we have now extended it to weakly compressible flow with slip. When setting $Ma = 0$ (incompressible), $u_s = 0$ (no-slip flow), and then (4.19) agrees with the results in [10]. Also, setting $\frac{dR}{dy} = 0$ as well, gives us the equation (3.20).

# Chapter 5

# Numerical Results

In this chapter, we give results for MPC simulations described in Chapter 3, and compare them to the analytical solution derived in Chapter 4. For the geometry (see equation 4.2), we fix $R_0 = 10.5$, $y_1 = 600.5$, $\delta \in [.5, 2.5]$, $l_1 + l_2 = 30$. For a symmetric geometry about $y_2$, $l_1 = 15 = l_2$, so by using $l_1 = 10, 20, 25$, we can asses the effect of an asymmetric stenosis. Varying $\delta$ from 0.5 to 2.5 allows variation of the degree of the constriction.

## 5.1 MPC Parameter values

We perform MPC simulations for the parameters $\rho$=20, $m = 1$, $k_BT = 1$, $\Delta t = 1$ and $a_0 = 1$ which gives us $\mu^{theo} = \mu_{kin} + \mu_{col} \approx 8.5994$ using (3.19). Thus, using $g = .005, .01, .02$ in (3.21) and (3.22), we expect $Re^{theo} \approx 3.91, 7.83, 15.65$ respectively. Based on our simulations ($g = .005, .01$ and $.02$) we found slightly faster or slower flow than predicted theoretically depending on the value of $\lambda$ used in the boundary condition (3.15), and thus computed the values of $Re^{num}$ by determining the average velocity $\overline{U}_0$ far upstream based on a quadratic fit to the numerical data. For example for $g = .005$, we find the best quadratic fit to the data to be:

$$p(x) = (-0.002336665428393)x^2 + (0.067822842877946)x - (-0.198040535417099) \tag{5.1}$$

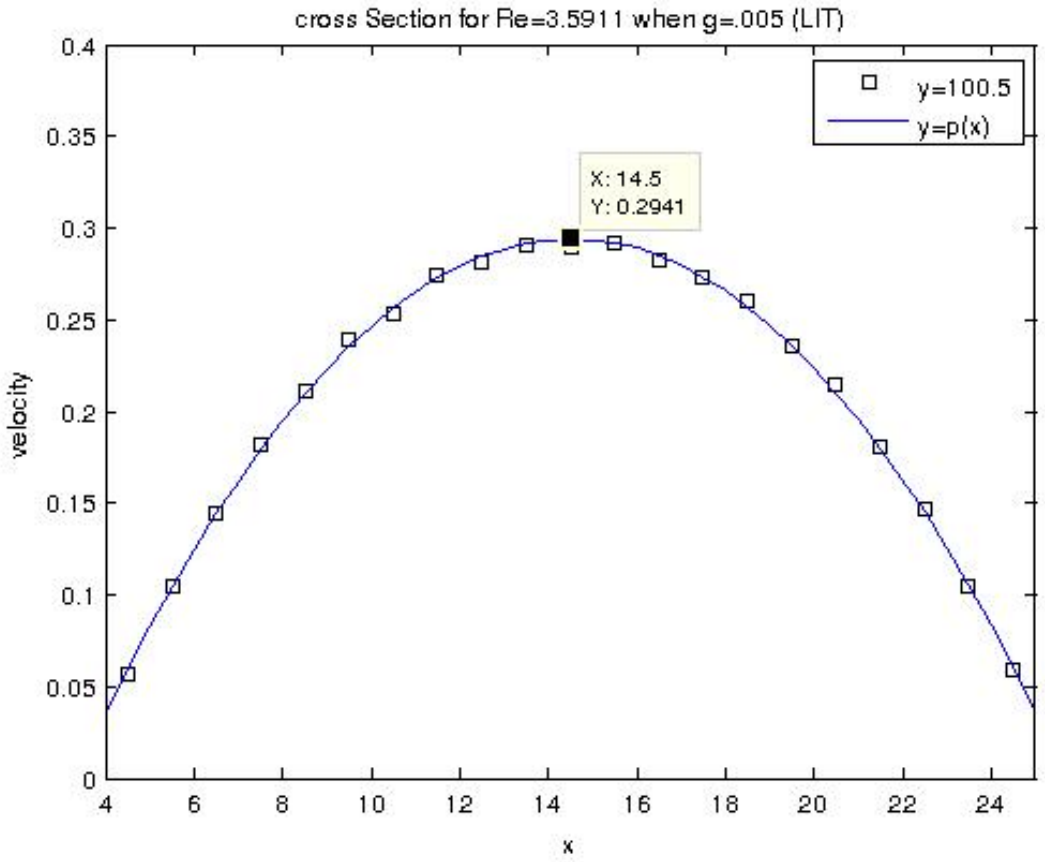


Figure 5.1: Cross Section Velocity profile far upstream with $\delta = .5$, $\lambda = .5$ and $l_1 = 20$

for $x \in [4, 25]$. Note that the $y$-axis is along the line $(x_c, z_c) = (14.5, 14.5)$, recalling $R_0 = 10.5$. This gives us $U_0^{num} \approx p(x)|_{x=14.5} \approx 0.2941$ leading to $Re_0^{num} = \frac{\overline{U}_0^{num} R_0}{\nu} = \frac{U_0^{num} R_0}{2\nu} \approx 3.5911$ according to (3.22). To determine the value of $u_s$, we evaluate $p$ at $x = 4$, giving $u_s^{num} \approx p(x)|_{x=4} \approx .0359$

Doing this in each case considered we can create the following table:

Table 5.1: Numerical and Analytical values of the parameter

| g | $\lambda$ | $\overline{U}_0^{num}$ | $u_s^{num}$ | $Re_0^{num}$ | $Re_0^{theo}$ |
|---|---|---|---|---|---|
| .005 | .5 | 0.147053389996745 | 0.035864189240397 | 3.591082785366538 | 3.91 |
| .005 | .4 | 0.143549086302675 | 0.024241689975924 | 3.505506759742446 | 3.91 |
| .005 | .2 | 0.150948849297109 | 0.008522004866408 | 3.686210934639019 | 3.91 |
| .005 | 0 | 0.168938215102946 | -0.003305017890580 | 4.125516018774997 | 3.91 |
| .01 | .5 | 0.294905743707093 | 0.073349242302891 | 7.201676476521217 | 7.83 |
| .01 | 0 | 0.338610045766604 | -0.007795888235905 | 8.268947124112849 | 7.83 |
| .02 | .5 | 0.597662347172252 | 0.145642488394896 | 14.595073030547203 | 15.65 |
| .02 | 0 | 0.683610724092895 | -0.019499224427164 | 16.693955190263139 | 15.65 |

For $R_0 = 10.5$, $\rho = 20$, $g = .005$, $\mu \approx 8.5994$, $\overline{U_0}^{num} = \frac{1}{2}U_0^{num} \approx .1471$ and $\sqrt{\frac{k_B T}{m}} = 1$, here is a specific example for the calculation of $Re_0^{num}$ and $Ma^{num}$ respectively:

$$\begin{aligned} Re_0^{num} &\approx \frac{\rho \overline{U}_0^{num} R_0}{\mu} \\ &\approx \frac{(20)(.1471)(10.5)}{8.5994} \\ &\approx 3.5911 \end{aligned}$$

and

$$\begin{aligned} Ma^{num} &= \frac{\overline{U}^{num}}{\sqrt{\frac{k_B T}{m}}} \\ &\approx \frac{\overline{U}_0}{\sqrt{k_B T}} \\ &\approx .1471 \end{aligned}$$

These values were then used in (4.20) together with $\rho \approx \rho_0$ and $\nu \approx \nu_0$, to obtain the analytical curves in the subsequent sections.

## 5.2 Results

### 5.2.1 Variation of Re

To vary the Reynolds number we vary $g(.005, .01$ and $.02)$ and consider a mild asymmetric stenosis with $\delta = .5$ and $l_1 = 20$. We consider both slip ($\lambda = .5$) and no-slip ($\lambda = 0$) boundary conditions.

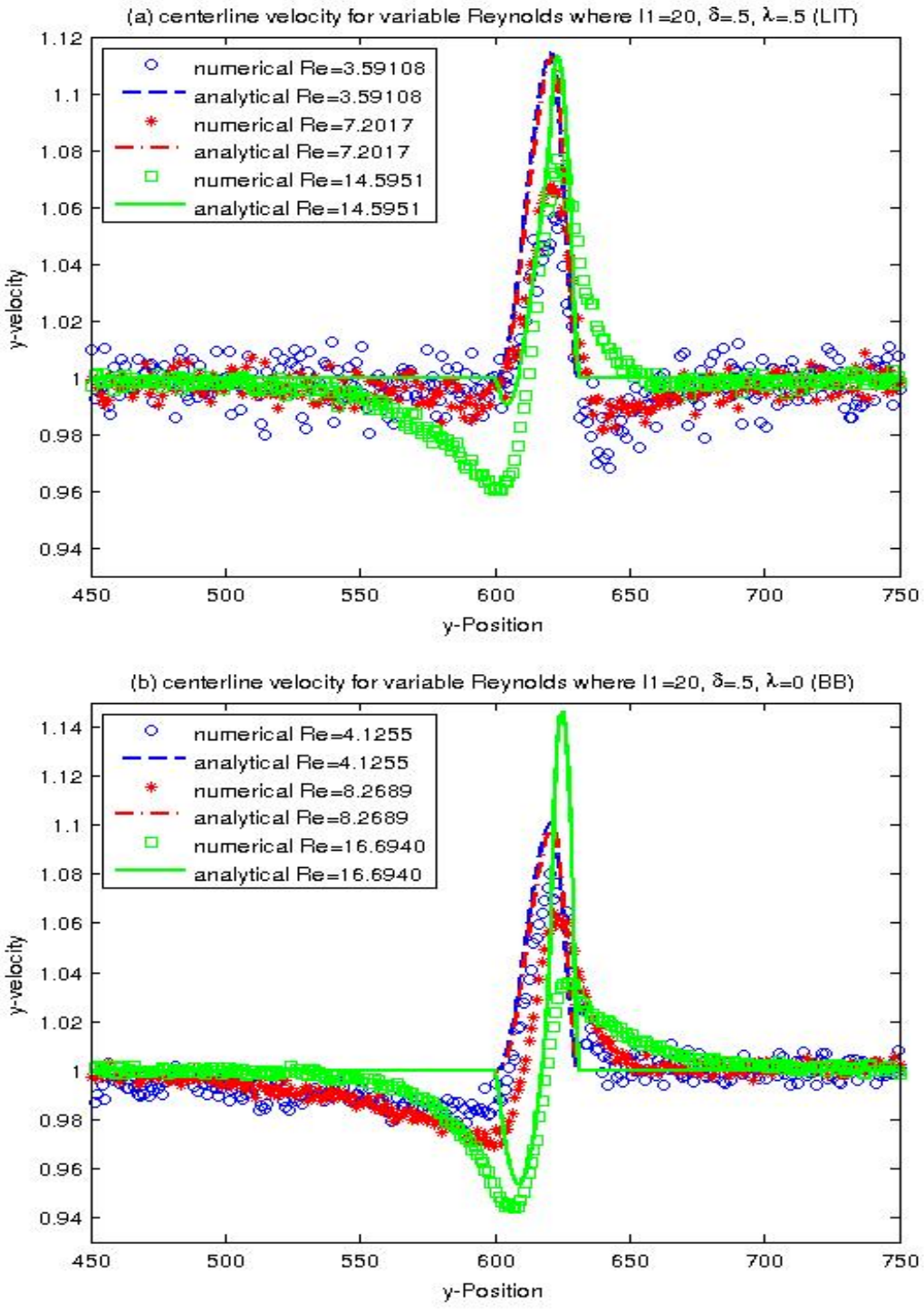


Figure 5.2: Scaled centerline velocity with $\delta = .5$, $l_1 = 20$ and (a) $\lambda = 0.5$ and (b) $\lambda = 0$

In Figure 5.2, we compare the numerical and analytical scaled centerline velocity profiles for different Reynolds numbers. In both figures we see that increasing the Reynolds number increases the flow velocity as expected. In flow with slip (Figure 5.2.(a)), the numerical results seems to be lower than the theoretical predictions for all Reynolds numbers considered, and for the largest Reynolds number ($Re = 14.6$) both the numerical and the analytical results show a pre-stenotic dip. However, the numerical results have a larger pre-stenotic dip than predicted theoretically. Furthurmore, the post-stenotic dip that is present in the numerical results for lower $Re$, is not present in the analytical curves.

As slip is removed, we see in Figure 5.2(b) that the numerical results have a pre-stenotic dip even for the smaller $Re$, lowering the speeds through the stenosis. For the larger Reynolds number $Re = 16.6940$, this dip agrees well with the analytical results although the analytical result has a higher peak than the numerical results.

In all cases considered, flow through the stenosis is slower in the numerical results compared to the theoretical predictions. Worth mentioning is the better agreement of analytical and numerical results in the no-slip case (Figure 5.2 (b)) compared to flow with slip (Figure 5.2 (a)).

### 5.2.2 Variation of $\delta$

To vary the degree of the stenosis, we vary $\delta$, fixing $g = .005$ in an asymmetric stenosis ($l_1 = 20$) with slip ($\lambda = .5$) and without slip ($\lambda = 0$). In Figure 5.3, we plot the scaled centerline velocity for both the numerical and analytical results. As the degree of constriction increases, the post-stenotic dip increases in the numerical curves in flow with slip (5.3 (a)) while there is more of a pre-stenotic dip in no-slip flow (5.3 (b)). In all cases considered, flow is faster through more severe stenoses, and numerical results give slower flow than predicted analytically. Also, the peaks of the numerical curves are slightly slower and to the right of the peaks of the analytical results. Again, there is better agreement between the analytical and numerical results in the no-slip case (5.3 (b)).

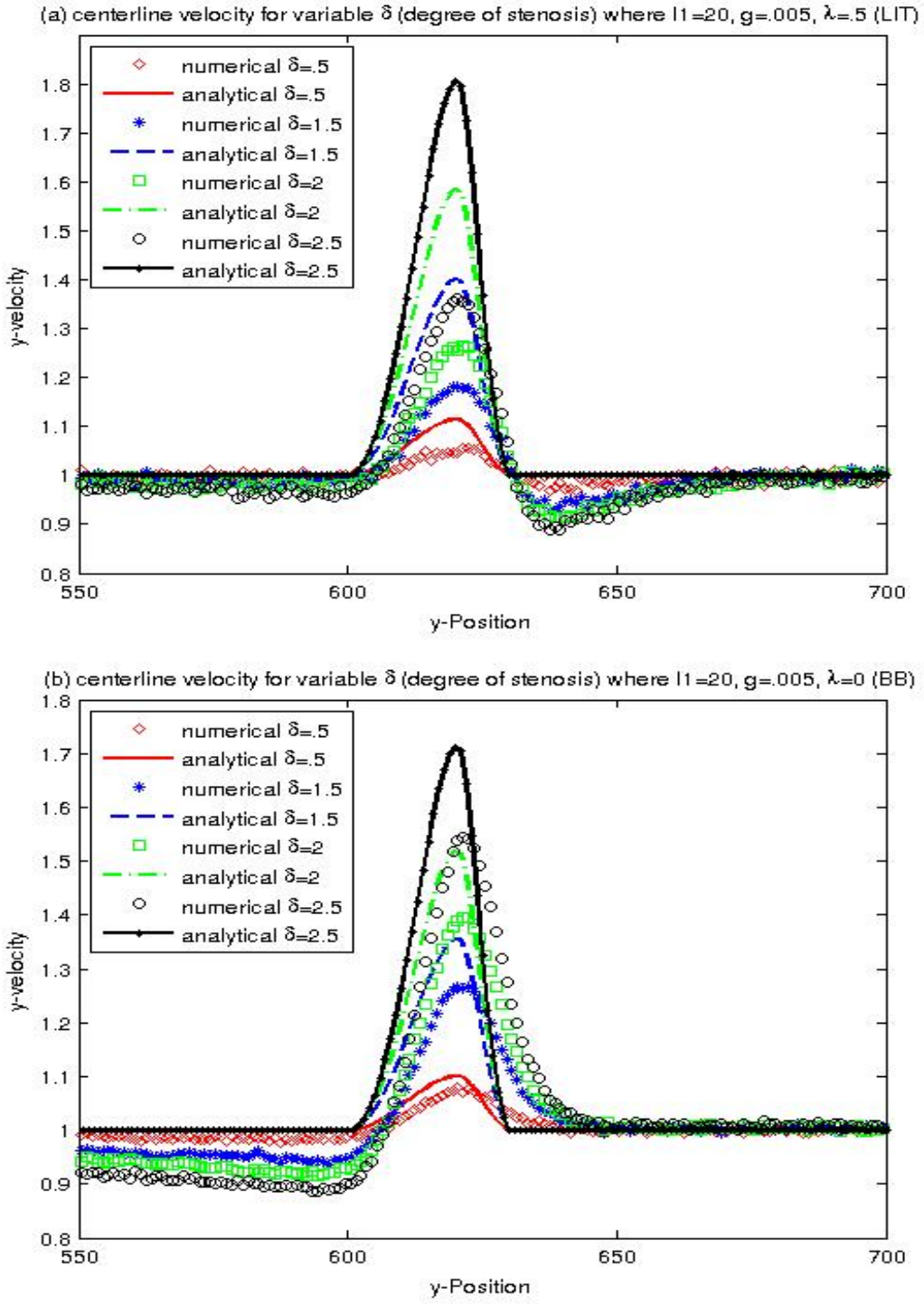


Figure 5.3: Scaled centerline velocity with $g = .005$, $l_1 = 20$ and (a) $\lambda = 0.5$ and (b) $\lambda = 0$

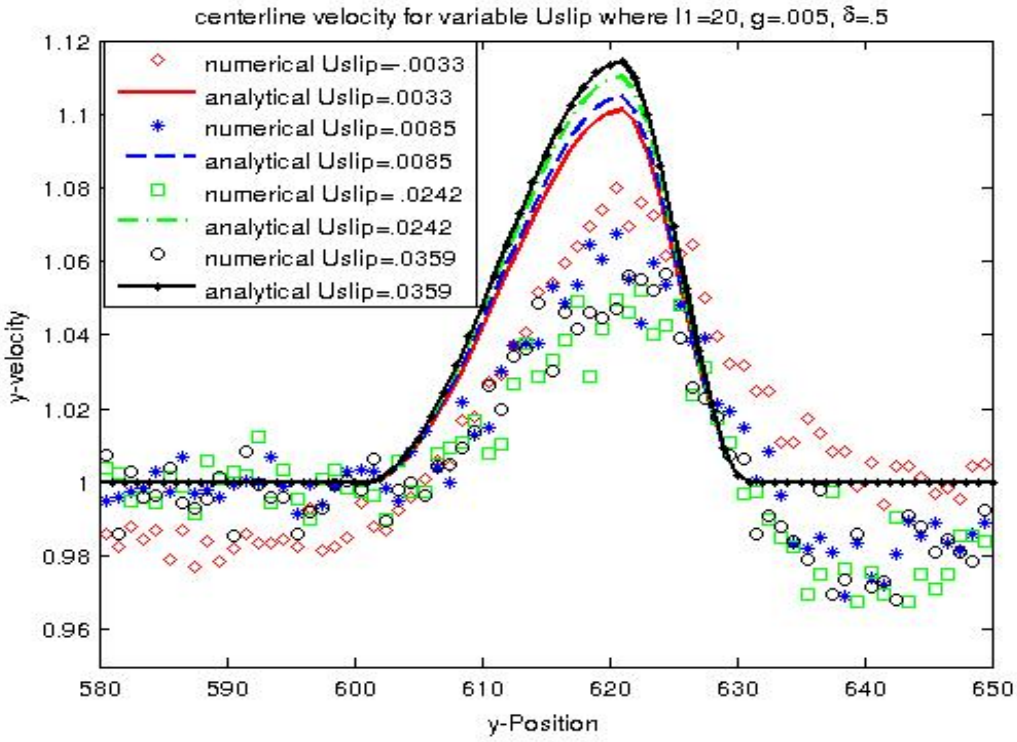


Figure 5.4: Scaled centerline velocity with $g = .005$, $\delta = .5$ and $l_1 = 20$

### 5.2.3 Variation of slip

To vary slip, we consider $\lambda = 0, 0.2, 0.4$ and $0.5$, fixing $g = .005$ and $\delta = 0.5$, in an asymmetric stenosis ($l_1 = 20$). Again the value of slip at the wall ($U_{slip}$) is estimated as per the discussion in section 5.1 (see also the table 5.1).

In Figure 5.4, we plot both numerical and analytical scaled centerline velocity profiles for various values of the slip parameter ($\lambda$). From the analytical curves it can be seen that increasing the slip increases the velocity through the constriction. On the contrary, as slip increases, the numerical results lead to a smaller pre-stenotic dip, relatively slower flow through the constriction, and more of a post-stenotic dip.

### 5.2.4 Variation of throat location

To asses the effect of asymmetry of the stenosis, we consider $l_1 = 10, 20$, and 25, fixing $g = .005$, in a mild stenosis ($\delta = .5$) with slip ($\lambda = .5$) in Figure 5.4 (a) and without slip ($\lambda$=0) in Figure 5.4 (b). We note that the peak of the analytical curves moves to the right as $l_1$ increases, and overpredicts the peaks of the numerical results. There is a fair bit of noise in the numerical data that makes it hard to see similar trends there, although the $l_1 = 10$ data points do have their peak further to the left. The numerical slip curves have post-stenotic dip, but the opposite is true for the no-slip numerical curves i.e there are pre-stenotic dips. Removing slip slows down the analytical velocity profiles whereas the opposite is true for the numerical velocity profiles.

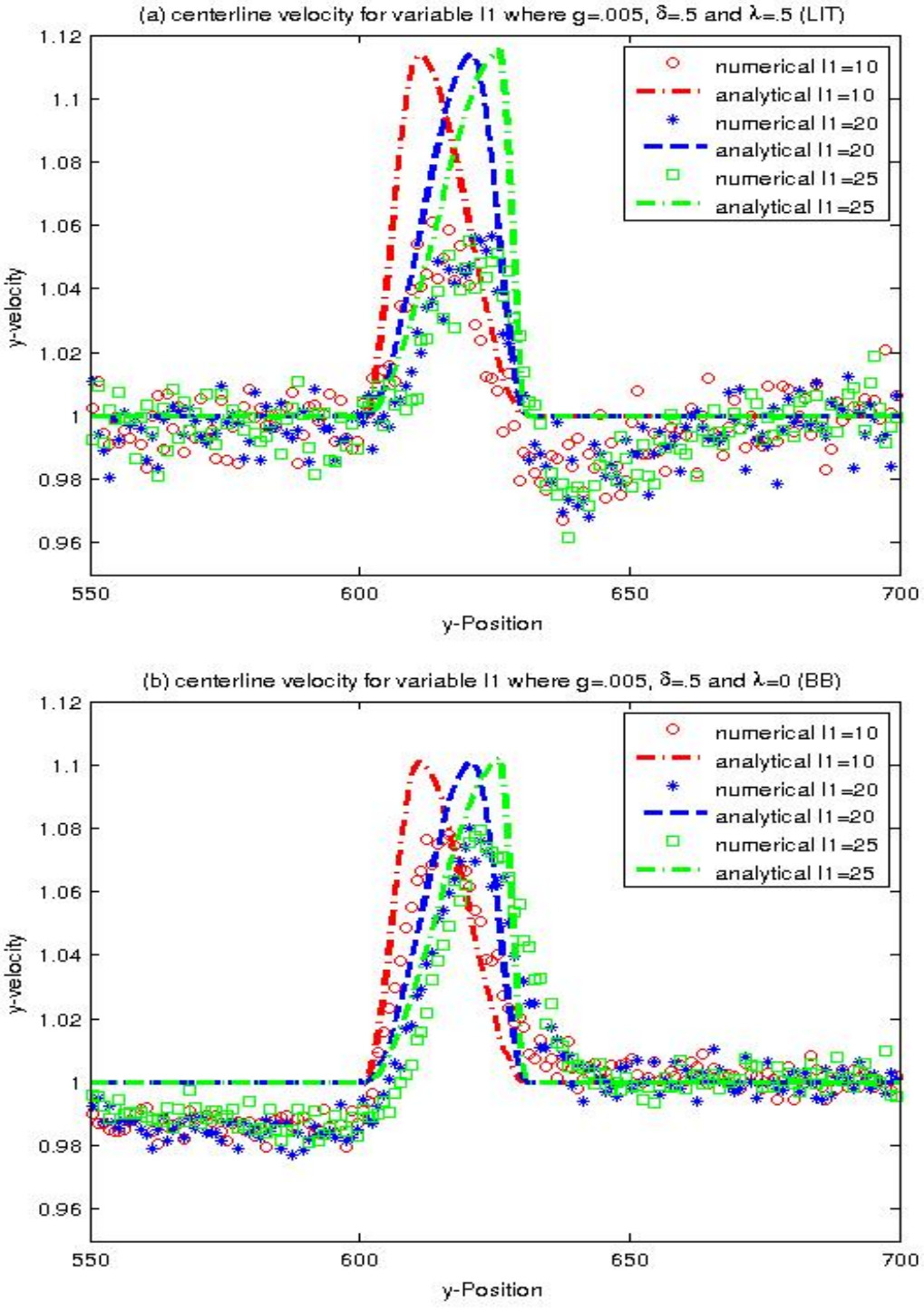


Figure 5.5: Scaled centerline velocity with $g = .005$, $\delta = .5$ and (a) $\lambda = 0.5$ and (b) $\lambda = 0$

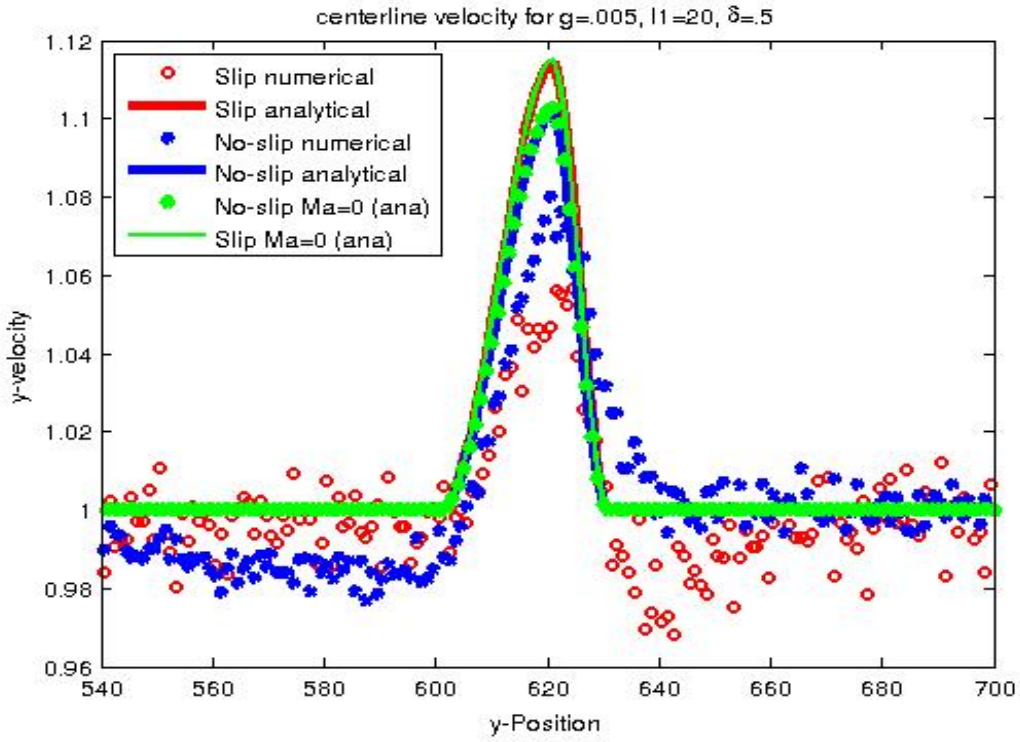


Figure 5.6: Scaled centerline velocity with $g = .005$, $\delta = .5$ and $l_1 = 20$

## 5.3 Role of Compressibility and Slip

In this section we investigate the role of compressibility and slip using the numerical and analytical results in a weakly compressible mild stenosis, in the case where the two have good agreement ($g = .005$, $\delta = .5$ and $l_1 = 20$).

In Figure 5.6 we compare the numerical results with slip and without, and compare them to the analytical predictions. Additionally, we plot the incompressible no-slip analytical curve so as to analyze the effect of compressibility and slip separately. From the figure we see that the analytical velocity profiles with slip are the fastest, where-as removing slip gives the slower flows. It seems that, numerically the opposite is true, that is slip flow is slower than no-slip flow. Worth noting is that compresibility ($Ma \neq 0$) does not seem to have as much of an effect, as the no-slip $Ma = 0$ curve overlaps the no-slip $Ma \neq 0$ curve, and likewise for slip ($Ma = 0$ or $Ma \neq 0$).

Figure 5.7 shows the contour plots for the analytical and numerical results with slip in both line and solid color. There is a shape difference between the analytical and the numerical contour lines, and also analytically it shows faster flow by the presence of the 1.1 contour. This comment is also true for the color contour. We see the faster flow in the center line from the darkest color, which is comparatively slow in the numerical color contour plot.

Figure 5.8 shows the contour plots for the analytical and numerical results without slip in both line and solid color. There is also a shape difference between the analytical and the numerical line contours. Again the analytical and numerical color contour have different flow rate along the center line, which can be seen from the color of the center.

Figure 5.9 shows the contour plots for the analytical results without slip and without compressibility (i.e $Ma = 0$) in both line and solid color. The line contour is very close to the line contour without slip where $Ma \neq 0$ (Fig. 5.8 (a-2)). From this we see that compressibility has less effect than slip analytically.

Finally, in Figure, 5.10, we plot scaled centerline density plots to check the $\rho \approx$constant assumption. We can see some variability in density, but note that the Reynolds number is fairly insensitive to these variations according to the expression given in section 5.1 ($\mu^{theo} = \mu_{kin} + \mu_{col} \approx 8.5994$), when used for $\frac{\mu}{\rho}$.

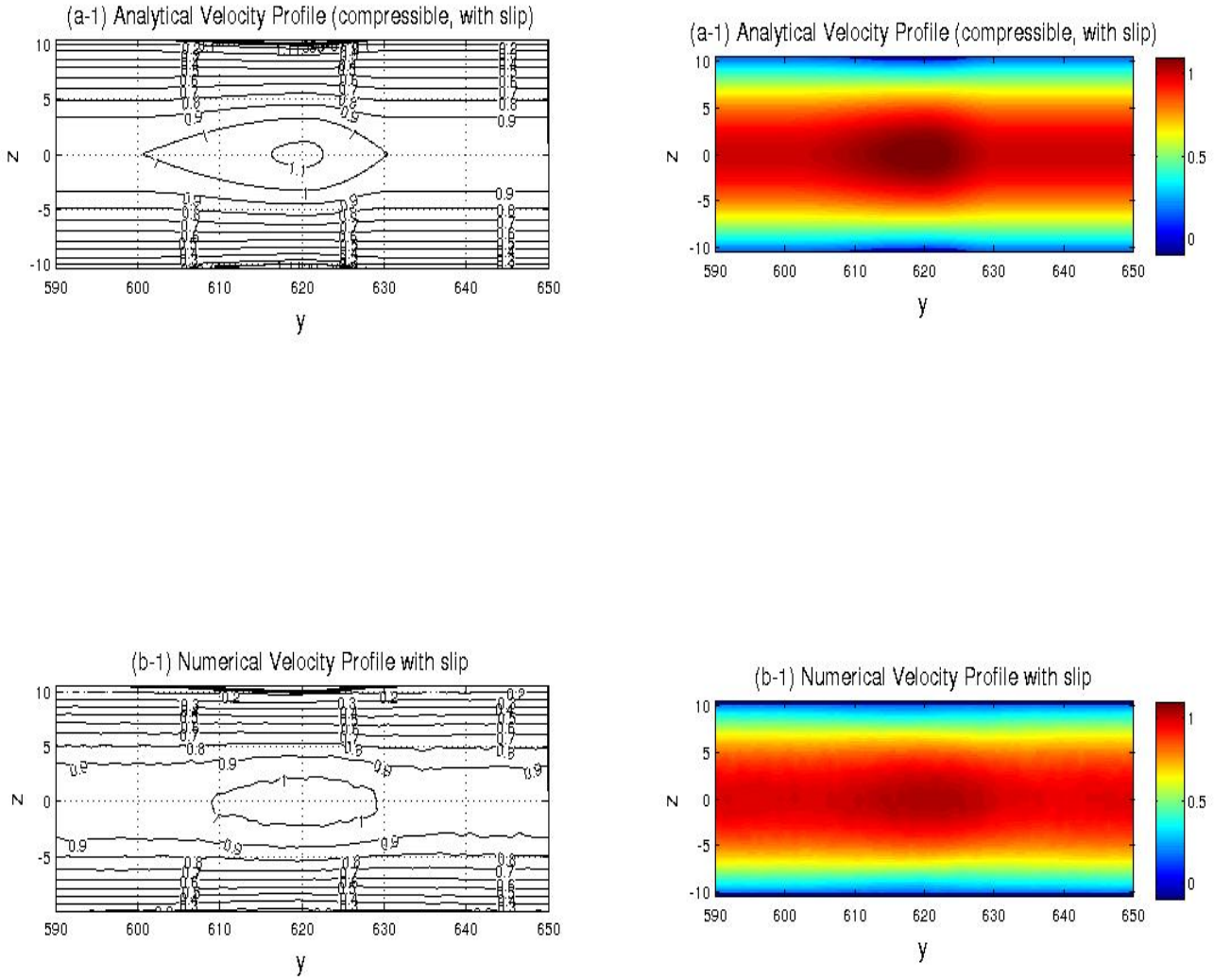


Figure 5.7: Analytical (a-1) and Numerical (b-1) Contour plot with slip for scaled velocity

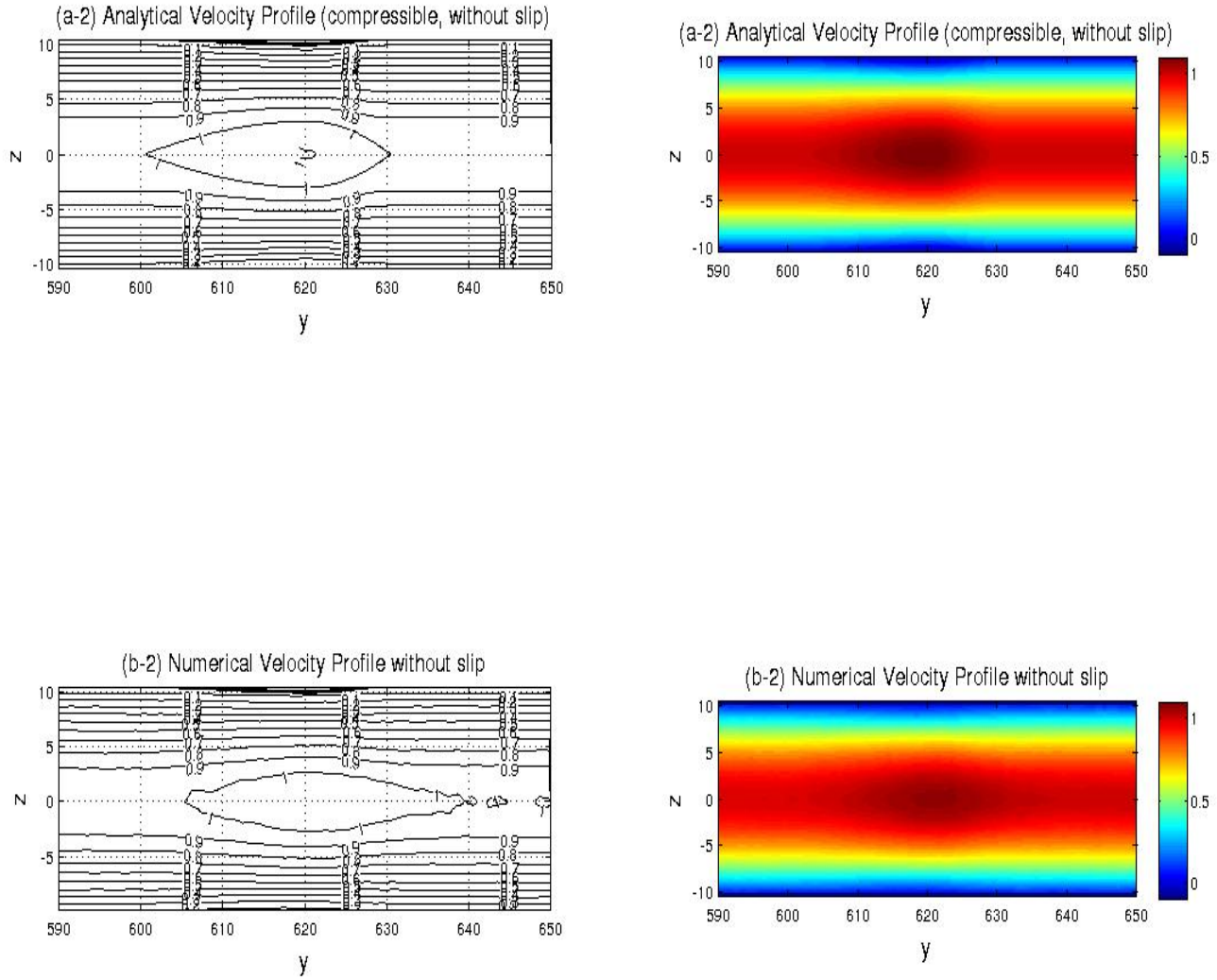


Figure 5.8: Analytical (a-2) and Numerical (b-2) Contour plot without slip for scaled velocity

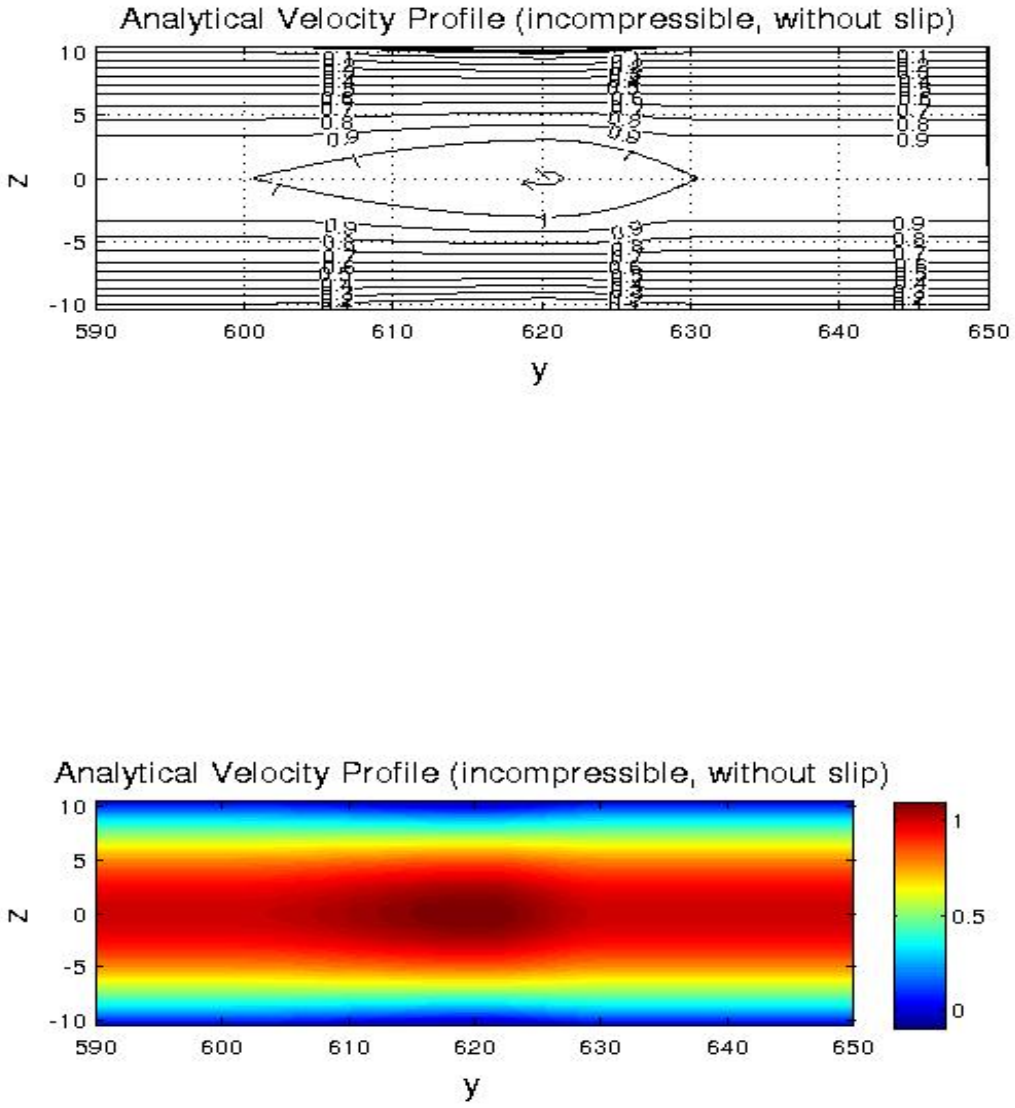


Figure 5.9: Contour plot with $g = .005$, $\delta = .5$, $Ma = 0$ and $\lambda = 0$ for scaled velocity

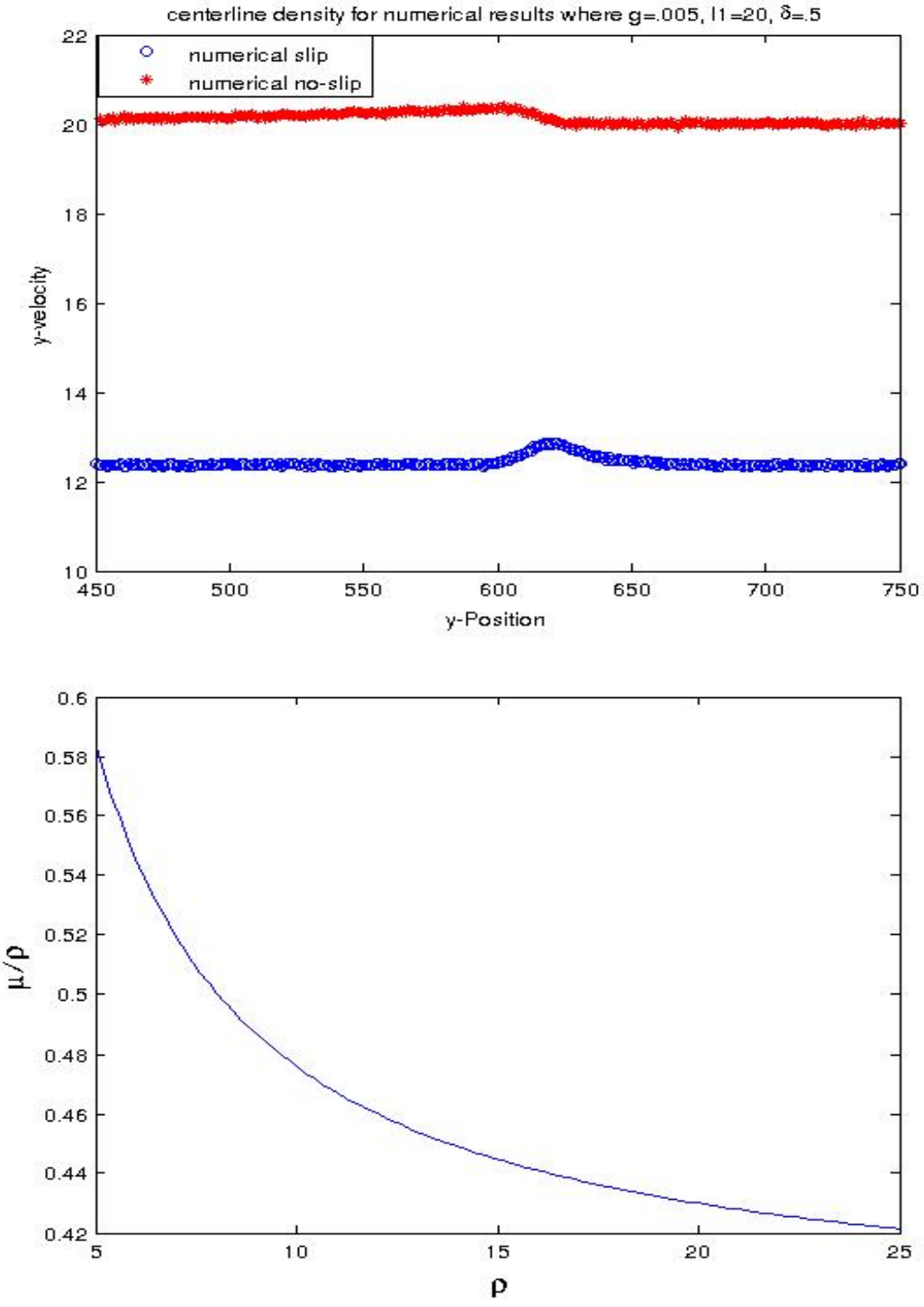


Figure 5.10: Scaled centerline density and $\rho$ against $\frac{\mu}{\rho}$

# Chapter 6

# Conclusions and Future Work

In this Thesis we have argued that slip and compressibility might be important in blood flow studies, and have investigated their role in a physiologically meaningful flow geometry (stenosis). In Chapter 4 we derived an approximate analytical velocity profile for flow of a weakly compressible fluid through an idealized flow geometry that we created so as to use it for axisymmetric flow through a mild asymmetric stenosis. In Chapter 5 we presented numerical results from particle-based (MPC) simulations through this flow geometry and compared it to the analytical approximation from Chapter 4. Comparisons between analytical and numerical results were made for various $Re$ and various flow geometries. In particular, we isolated the role of slip and compressibility in flow through a geometry where the numerical and analytical results were in fairly good agreement.

Although some features are not captured by the analytical approximation, the analytical and the numerical results are in fairly good agreement when the Mach number is small (weakly compressible) and $\delta$ is small (mild stenosis). In this flow geometry we found that adding slip causes a distinct effect analytically, while the effect of compressibility is not as great. Numerically there are significant effects of slip and compressibility, although it is not possible to remove compressibility in the MPC flow.

In general, the analytical results overpredicted the numerical results, and pre- and post-stenotic dips present in the numerical results were not present in the analytical results except in one case (see Fig. 5.2(b)) where the analytical results also had a pre-stenotic dip for the highest Reynolds number considered. Furthermore, the analytical and numerical results were in better agreement when there was no slip at the wall, and in a mild stenosis. The analytical results showed a distinct dependence on

the asymmetry of the stenosis, although this dependence was less pronounced in the numerical results. Finally, flow seems to increase with slip in the analytical results (as expected), while the opposite is observed (Fig. 5.4) in the numerical results. This latter counter-intuitive finding might be a consequence of the thermostat which ensures a fixed temperature in the system that — as slip increases — might lower the centerline velocity, and thus lead to a slower rather than faster flow. As such, the interpretation of the numerical results needs to be looked at more closely prior to forming further conclusions.

For higher Reynolds numbers, and for more severe stenoses, agreement between analytical and numerical results are found to be worse. One way that better agreement might be found is in relaxing the $\rho \approx \rho_0$=constant assumption in the analytical approximation and hence also the $\mu \approx \mu_0$=constant assumptions. This is currently under investigation. Additionally, as there is some noise in the data for some of the numerical results (see Figure 5.5 in particular) it might be better to determine the values in Table 5.1 not from a single cross-section as per the section 5.1 discussion, but rather scale by an average over several hundred cross-sections upstream and letting the simulations run even longer, so as to see if the noise is inherent to the system, or if the system has not yet fully reached equilibrium. This too is currently under investigation.

# Appendix A

# Appendix

In this Appendix we provide the details of the calculations (4.7)-(4.9) to equation (4.10). The continuity equation (4.7) is:

$$\begin{aligned}
&\tfrac{1}{r}\tfrac{\partial(\rho r v)}{\partial r} + \tfrac{\partial(\rho u)}{\partial y} = 0 \\
&\Rightarrow \tfrac{1}{r}\tfrac{\partial(\rho r v)}{\partial r} = -\tfrac{\partial(\rho u)}{\partial y} \\
&\Rightarrow \tfrac{1}{r}\rho r\tfrac{\partial(v)}{\partial r} + \tfrac{1}{r}\rho v = -\tfrac{\partial(\rho u)}{\partial y} \\
&\Rightarrow \rho\Big(\tfrac{\partial v}{\partial r} + \tfrac{1}{r}v\Big) = -\tfrac{\partial(\rho u)}{\partial y} \\
&\Rightarrow \tfrac{\partial v}{\partial r} + \tfrac{1}{r}v = -\tfrac{1}{\rho}\tfrac{\partial(\rho u)}{\partial y} \\
&\Rightarrow \tfrac{\partial}{\partial y}\Big(\tfrac{\partial v}{\partial r} + \tfrac{1}{r}v\Big) = -\tfrac{\partial}{\partial y}\Big(\tfrac{1}{\rho}\tfrac{\partial(\rho u)}{\partial y}\Big)
\end{aligned} \tag{A.1}$$

Using (A.1) in equation (4.8) we have the equation:

$$\begin{aligned}
&\rho\left(v\tfrac{\partial u}{\partial r} + u\tfrac{\partial u}{\partial y}\right) = -\tfrac{\partial p}{\partial y} + \mu\left(\tfrac{4}{3}\tfrac{\partial^2 u}{\partial y^2} + \tfrac{\partial^2 u}{\partial r^2} + \tfrac{1}{3}\tfrac{\partial^2 v}{\partial y \partial r} + \tfrac{1}{3r}\tfrac{\partial v}{\partial y} + \tfrac{1}{r}\tfrac{\partial u}{\partial r}\right) + F_y \\
&\Rightarrow u\tfrac{\partial u}{\partial y} = -\tfrac{1}{\rho}\tfrac{\partial p}{\partial y} + \nu\left(\tfrac{4}{3}\tfrac{\partial^2 u}{\partial y^2} + \tfrac{\partial^2 u}{\partial r^2} + \tfrac{1}{r}\tfrac{\partial u}{\partial r} - \tfrac{1}{3}\tfrac{\partial}{\partial y}\Big(\tfrac{1}{\rho}\tfrac{\partial}{\partial y}(\rho u)\Big)\right) + g
\end{aligned} \tag{A.2}$$

where we have neglected the term $v\frac{\partial u}{\partial r}$ as flow in the radial direction is assumed to be negligible compared to the flow in the $y$ direction, and changes of flow in the $y$ direction depends on changes in $y$ more than changes in radius. From this concept it can be assumed that $v\frac{\partial u}{\partial r} \ll u\frac{\partial u}{\partial y}$, and thus, we neglect the term

$v\frac{\partial u}{\partial r}$. Multiplying (A.2) by $r$ and then integrating accross the tube with respect to $r$ from 0 to $R$ we get:

$$\begin{aligned}
&\textstyle\int_0^R ru\frac{\partial u}{\partial y}dr = \int_0^R \Big[ -\frac{1}{\rho}r\frac{\partial p}{\partial y} + \nu\left(\frac{4}{3}r\frac{\partial^2 u}{\partial y^2} + r\frac{\partial^2 u}{\partial r^2} + \frac{\partial u}{\partial r} - \frac{1}{3}r\frac{\partial}{\partial y}\left(\frac{1}{\rho}\frac{\partial}{\partial y}(\rho u)\right)\right) + gr\Big]dr \\
&\Rightarrow \tfrac{1}{2}\tfrac{d}{dy}\textstyle\int_0^R ru^2dr = -\frac{1}{\rho}\frac{dp}{dy}\frac{R^2}{2} + g\frac{R^2}{2} + \nu\int_0^R \frac{\partial}{\partial r}\big(r\frac{\partial u}{\partial r}\big)dr \\
&\qquad\qquad + \nu\textstyle\int_0^R \Big[\frac{4}{3}r\frac{\partial^2 u}{\partial y^2} - \frac{r}{3}\frac{\partial}{\partial y}\big(\frac{1}{\rho}\rho\frac{\partial u}{\partial y} + \frac{1}{\rho}\frac{\partial \rho}{\partial y}u\big)\Big]dr \\
&\Rightarrow \tfrac{1}{2}\tfrac{d}{dy}\textstyle\int_0^R ru^2dr = -\frac{1}{\rho}\frac{dp}{dy}\frac{R^2}{2} + g\frac{R^2}{2} + \nu R\Big(\frac{\partial u}{\partial r}\Big)_R \\
&\qquad\qquad + \nu\textstyle\int_0^R r\frac{\partial^2 u}{\partial y^2}dr - \frac{\nu}{3}\frac{\partial}{\partial y}\big(\frac{1}{\rho}\frac{\partial \rho}{\partial y}\big)\int_0^R rudr \\
&\Rightarrow \tfrac{1}{2}\tfrac{d}{dy}\textstyle\int_0^R ru^2dr = -\frac{1}{\rho}\frac{dp}{dy}\frac{R^2}{2} + g\frac{R^2}{2} + \nu R\Big(\frac{\partial u}{\partial r}\Big)_R \\
&\qquad\qquad + \nu\frac{d^2}{dy^2}\textstyle\int_0^R rudr - \frac{\nu}{3}\frac{\partial}{\partial y}\big(\frac{1}{\rho}\frac{\partial \rho}{\partial y}\big)\int_0^R rudr \\
&\Rightarrow \tfrac{1}{2}\tfrac{d}{dy}\textstyle\int_0^R ru^2dr = -\frac{1}{\rho}\frac{dp}{dy}\frac{R^2}{2} + g\frac{R^2}{2} + \nu R\Big(\frac{\partial u}{\partial r}\Big)_R \\
&\qquad\qquad + \nu\frac{d^2}{dy^2}\Big(\frac{\pi R^2\overline{U}}{2\pi}\Big) - \frac{\nu}{3}\frac{\partial}{\partial y}\big(\frac{1}{\rho}\frac{\partial \rho}{\partial y}\big)\Big(\frac{\pi R^2\overline{U}}{2\pi}\Big)
\end{aligned} \tag{A.3}$$

where we have used $\int rudr = \left(\frac{\pi R^2\overline{U}}{2\pi}\right)$ from (4.11)[10]. Note that by (4.9), $\frac{\partial p}{\partial r} = 0$, which means that $p = p(y)$.

# Appendix B

# Appendix

In this Appendix we provide the details for some of the lengthy calculations leading to results in Chapter 4.

## B.1 Calculation of velocity

In this section, we show how (4.11)-(4.14) lead to (4.15). We have the equation $Q = \pi\rho R^2\overline{U} = \int_0^R 2\pi\rho r u dr \rightarrow$(4.11)
and the equation $\frac{u}{U} = A\eta + B\eta^2 + C\eta^3 + D\eta^4 + E \rightarrow$(4.12) where $\eta = \left(1 - \frac{r}{R}\right)$. Now substituting (4.12)

in (4.11) we get:

$$
\begin{aligned}
Q = \pi\rho R^2\overline{U} &= \textstyle\int_0^R 2\pi\rho r u dr \\
&= \textstyle\int_0^R 2\pi\rho r U\Big(A\eta + B\eta^2 + C\eta^3 + D\eta^4 + E\Big)dr \\
&= 2\pi\rho U\Big[A\textstyle\int_0^R \big(r - \frac{r^2}{R}\big)dr + B\int_0^R \big(r - \frac{2r^2}{R} + \frac{r^3}{R^2}\big)dr \\
&+ C\textstyle\int_0^R \big(r - \frac{3r^2}{R} + \frac{3r^3}{R^2} - \frac{r^4}{R^3}\big)dr + D\int_0^R \big(r - \frac{4r^2}{R} + \frac{6r^3}{R^2} - \frac{4r^4}{R^3} + \frac{r^5}{R^4}\big)dr \\
&+ E\textstyle\int_0^R r dr\Big] \\
&= 2\pi\rho U\Bigg[\big(A + B + C + D + E\big)\textstyle\int_0^R r dr - \big(A + 2B + 3C + 4D\big)\int_0^R \frac{r^2}{R}dr \\
&+ \big(B + 3C + 6D\big)\textstyle\int_0^R \frac{r^3}{R^2}dr - \big(C + 4D\big)\int_0^R \frac{r^4}{R^3}dr + D\int_0^R \frac{r^5}{R^4}dr \\
&= 2\pi\rho U\Bigg[\big(A + B + C + D + E\big)\tfrac{R^2}{2} - \big(A + 2B + 3C + 4D\big)\tfrac{R^2}{3} \\
&+ \big(B + 3C + 6D\big)\tfrac{R^2}{4} - \big(C + 4D\big)\tfrac{R^2}{5}dr + D\tfrac{R^2}{6}\Bigg] \\
&= 2\pi\rho U R^2\Bigg[\tfrac{A}{6} + \tfrac{B}{12} + \tfrac{C}{20} + \tfrac{D}{30} + \tfrac{E}{2}\Bigg] \\
&= 2\pi\rho U R^2\Bigg[\Bigg(\tfrac{-\lambda+10-12E+\tilde{T}}{42}\Bigg) + \Bigg(\tfrac{3\lambda+5-6E-3\tilde{T}}{84}\Bigg) \\
&+ \Bigg(\tfrac{-3\lambda-12+20E+3\tilde{T}}{140}\Bigg) + \Bigg(\tfrac{\lambda+4-9E-\tilde{T}}{210}\Bigg) + \tfrac{E}{2}\Bigg] \qquad \text{using (4.13)} \\
\Rightarrow \pi\rho R^2\overline{U} &= \tfrac{2\pi\rho U R^2}{420}\Big(-2\lambda + 2\tilde{T} + 97 + 102E\Big) \\
\Rightarrow \overline{U} &= \tfrac{U}{210}\Big[97 - 2\big(\lambda - \tilde{T}\big) + 102E\Big] \\
\Rightarrow \overline{U} &= \tfrac{97}{210}U - \tfrac{U}{105}\Bigg(\tfrac{dp}{dy}\tfrac{R^2}{\mu U} - \tfrac{gR^2}{\nu U}\Bigg) + \tfrac{102}{210}UE \qquad \text{using (4.14)}
\end{aligned}
\tag{B.1}
$$

$$
\begin{aligned}
&\Rightarrow \overline{U} = \tfrac{97}{210}U - \tfrac{R^2}{105}\Bigg(\tfrac{1}{\mu}\tfrac{dp}{dy} - \tfrac{g}{\nu}\Bigg) + \tfrac{102}{210}UE \\
&\Rightarrow \overline{U} = \tfrac{97}{210}U - \tfrac{R^2}{105}\Bigg(\tfrac{1}{\mu}\tfrac{dp}{dy} - \tfrac{g}{\nu}\Bigg) + \tfrac{17}{35}\tfrac{u_s}{\sqrt{1+R'(y)^2}} \\
&\Rightarrow \tfrac{97}{210}U = \overline{U} + \tfrac{R^2}{105}\Bigg(\tfrac{1}{\mu}\tfrac{dp}{dy} - \tfrac{g}{\nu}\Bigg) - \tfrac{17}{35}\tfrac{u_s}{\sqrt{1+R'(y)^2}} \\
&\Rightarrow U = \tfrac{210}{97}\Big(\tfrac{Q}{\rho\pi R^2}\Big) + \tfrac{2}{97}R^2\Big(\tfrac{1}{\mu}\tfrac{dp}{dy} - \tfrac{g\rho}{\mu}\Big) - \tfrac{102}{97}\tfrac{u_s}{\sqrt{1+R'(y)^2}} \\
&\Rightarrow U = \tfrac{210}{97\pi R^2}\tfrac{Q}{\rho} + \tfrac{2}{97}\tfrac{R^2}{\mu}\tfrac{dp}{dy} - \tfrac{2R^2\rho g}{97\mu} - \tfrac{102}{97}\tfrac{u_s}{\sqrt{1+R'(y)^2}}
\end{aligned}
\tag{B.2}
$$

This is equation (4.15) as desired.

## B.2 Derivation of equation (4.18)

In this section, we show that how equation (4.10) becomes (4.18). We have the equation (4.10) as the following:

$$\begin{aligned}\tfrac{1}{2}\tfrac{d}{dy}\int_0^R ru^2dr = &-\tfrac{1}{\rho}\tfrac{dp}{dy}\tfrac{R^2}{2} + g\tfrac{R^2}{2} + \nu R\Big(\tfrac{\partial u}{\partial r}\Big)_R \\ &+ \nu\tfrac{d^2}{dy^2}\Big(\tfrac{\pi R^2\overline{U}}{2\pi}\Big) - \tfrac{\nu}{3}\tfrac{\partial}{\partial y}\big(\tfrac{1}{\rho}\tfrac{\partial\rho}{\partial y}\big)\Big(\tfrac{\pi R^2\overline{U}}{2\pi}\Big)\end{aligned}$$

Now we use the concept that the velocity profile is approximately parabolic i.e $u = 2\overline{U}\big[1-\big(\tfrac{r}{R}\big)^2\big]$ in the left hand side of the equation which gives us the following:

$$\begin{aligned}&\tfrac{1}{2}\tfrac{d}{dy}\int_0^R 4r\overline{U}^2\big(1-\tfrac{2r^2}{R^2}+\tfrac{r^4}{R^4}\big)dr \\ &= 2\tfrac{d}{dy}\overline{U}^2\int_0^R\left(r-\tfrac{2r^3}{R^2}+\tfrac{r^5}{R^4}\right)dr \\ &= 2\tfrac{d}{dy}\overline{U}^2\left(\tfrac{r^2}{2}-\tfrac{2r^4}{4R^2}+\tfrac{r^6}{6R^4}\right)\Bigg|_0^R \\ &= 2\tfrac{d}{dy}\overline{U}^2\left(\tfrac{R^2}{2}-\tfrac{R^2}{2}+\tfrac{R^2}{6}\right) \\ &= 2\tfrac{d}{dy}\left(\tfrac{1}{6}\overline{U}^2R^2\right) \\ &= \tfrac{d}{dy}\left(\tfrac{1}{3}\overline{U}^2R^2\right)\end{aligned} \tag{B.3}$$

Now we can write equation (B.3) in the following form:

$$\frac{d}{dy}\left(\frac{1}{3}\overline{U}^2R^2\right) = -\frac{1}{\rho}\frac{dp}{dy}\frac{R^2}{2} + g\frac{R^2}{2} + \nu R\Big(\frac{\partial u}{\partial r}\Big)_R + \nu\frac{d^2}{dy^2}\Big(\frac{R^2\overline{U}}{2}\Big) - \frac{\nu}{3}\frac{\partial}{\partial y}\Big(\frac{1}{\rho}\frac{\partial\rho}{\partial y}\Big)\Big(\frac{R^2\overline{U}}{2}\Big) \tag{B.4}$$

Now from (4.12),

$$\begin{aligned}
\Big(\tfrac{\partial u}{\partial r}\Big)_R &= \tfrac{\partial}{\partial r}\Bigg(U\big(A\eta + B\eta^2 + C\eta^3 + D\eta^4 + E\big)\Bigg)_R \\
&= \Bigg[UA\tfrac{\partial}{\partial r}\big(1-\tfrac{r}{R}\big) + UB\tfrac{\partial}{\partial r}\big(1-\tfrac{r}{R}\big)^2 + UC\tfrac{\partial}{\partial r}\big(1-\tfrac{r}{R}\big)^3 \\
&\quad + UD\tfrac{\partial}{\partial r}\big(1-\tfrac{r}{R}\big)^4 + UE\tfrac{\partial}{\partial r}\big(1\big)\Bigg]\Bigg|_R \\
&= UA\big(-\tfrac{1}{R}\big) + UB\big(2\big(1-\tfrac{r}{R}\big)\big(-\tfrac{1}{R}\big)\big)_R + UC\big(3\big(1-\tfrac{r}{R}\big)^2\big(-\tfrac{1}{R}\big)\big)_R \\
&\quad + UD\big(4\big(1-\tfrac{r}{R}\big)^3\big(-\tfrac{1}{R}\big)\big)_R + 0 \\
\Rightarrow \Big(\tfrac{\partial u}{\partial r}\Big)_R &= -\tfrac{UA}{R}
\end{aligned}$$

Now equation (B.4) becomes:

$$\begin{aligned}
\tfrac{d}{dy}\Bigg(\tfrac{1}{3}\overline{U}^2R^2\Bigg) &= -\tfrac{1}{\rho}\tfrac{dp}{dy}\tfrac{R^2}{2} + g\tfrac{R^2}{2} + \nu R\Big(-\tfrac{UA}{R}\Big) \\
&\quad + \nu\tfrac{d^2}{dy^2}\Big(\tfrac{R^2\overline{U}}{2}\Big) - \tfrac{\nu}{3}\tfrac{\partial}{\partial y}\Big(\tfrac{1}{\rho}\tfrac{\partial\rho}{\partial y}\Big)\Big(\tfrac{R^2\overline{U}}{2}\Big) \\
\Rightarrow \tfrac{d}{dy}\Bigg(\tfrac{1}{3}\tfrac{R^2Q^2}{\pi^2\rho^2R^4}\Bigg) &= -\tfrac{1}{\rho}\tfrac{dp}{dy}\tfrac{R^2}{2} + g\tfrac{R^2}{2} + \nu U\Big(-\tfrac{\lambda+10+\tilde{T}-12E}{7}\Big) \\
&\quad + \nu\tfrac{d^2}{dy^2}\Big(\tfrac{Q}{2\pi\rho}\Big) - \tfrac{\nu}{3}\tfrac{\partial}{\partial y}\Big(\tfrac{1}{\rho}\tfrac{\partial\rho}{\partial y}\Big)\Big(\tfrac{Q}{2\pi\rho}\Big) \qquad \text{using (4.11) and (4.13)} \\
\Rightarrow \tfrac{1}{3\pi^2}\tfrac{d}{dy}\Bigg(\tfrac{Q^2}{\rho^2R^2}\Bigg) &= -\tfrac{1}{\rho}\tfrac{dp}{dy}\tfrac{R^2}{2} + g\tfrac{R^2}{2} + \tfrac{U}{7}\tfrac{\mu}{\rho}\tfrac{dp}{dy}\tfrac{R^2}{\mu U} \\
&\quad - \tfrac{\nu U}{7}\tfrac{gR^2}{\nu U} - \tfrac{10\nu U}{7} + \tfrac{12\nu U}{7}\tfrac{u_s}{U\sqrt{1+R'^2(y)}} \qquad \text{using (4.14)} \\
&\quad + \tfrac{\nu}{2\pi}\tfrac{d^2}{dy^2}\tfrac{Q}{\rho} - \tfrac{\nu}{6\pi}\tfrac{\partial}{\partial y}\Big(\tfrac{1}{\rho}\tfrac{\partial\rho}{\partial y}\Big)\tfrac{Q}{\rho}
\end{aligned} \tag{B.5}$$

Now

$$\begin{aligned}
\tfrac{d}{dy}\Bigg(\tfrac{Q^2}{\rho^2R^2}\Bigg) &= \tfrac{d}{dy}\big(Q^2\rho^{-2}R^{-2}\big) \\
&= 2Q\tfrac{dQ}{dy}\rho^{-2}R^{-2} + Q^2\big(-2\rho^{-3}\tfrac{d\rho}{dy}\big)R^{-2} + Q^2\rho^{-2}\big(-2R^{-3}\big)\tfrac{dR}{dy} \\
&= \tfrac{2Q}{\rho^2R^2}\tfrac{dQ}{dy} - \tfrac{2Q^2}{\rho^3R^2}\tfrac{d\rho}{dy} - \tfrac{2Q^2}{\rho^2R^3}\tfrac{dR}{dy} \\
&= \tfrac{2Q}{\rho^2R^2}\tfrac{dQ}{dy} - \tfrac{2Q^2}{\rho^3R^2}\tfrac{m}{k_BT}\tfrac{dp}{dy} - \tfrac{2Q^2}{\rho^2R^3}\tfrac{dR}{dy}
\end{aligned} \tag{B.6}$$

using $\frac{dQ}{dy} = 0$ and $\frac{d\rho}{dy} = \frac{dp}{dy}\left(\frac{m}{k_B T}\right)$. Now

$$\begin{aligned}\frac{d^2}{dy^2}\left(\frac{Q}{\rho}\right) &= \frac{d^2}{dy^2}\left(Q\rho^{-1}\right)\\ &= \frac{d}{dy}\left(\rho^{-1}\frac{dQ}{dy} + Q(-1)\rho^{-2}\frac{d\rho}{dy}\right)\\ &= \frac{d}{dy}\left(-\frac{Q}{\rho^2}\frac{d\rho}{dy}\right)\end{aligned} \tag{B.7}$$

and

$$\begin{aligned}\frac{d}{dy}\left(-Q\rho^{-2}\frac{d\rho}{dy}\right) &= -\frac{dQ}{dy}\rho^{-2}\frac{d\rho}{dy} - Q(-2)\rho^{-3}\left(\frac{d\rho}{dy}\right)^2 - Q\rho^{-2}\frac{d^2\rho}{dy^2}\\ &= \frac{2Q}{\rho^3}\left(\frac{d\rho}{dy}\right)^2 - \frac{Q}{\rho^2}\frac{d^2\rho}{dy^2}\\ &= \frac{2Qm^2}{\rho^3 k_B^2 T^2}\left(\frac{dp}{dy}\right)^2 - \frac{Q}{\rho^2}\frac{d^2\rho}{dy^2}\end{aligned} \tag{B.8}$$

Substituting equation (B.6) and (B.8) into (B.5) and by neglecting the higher derivative of $p$ as well as the $\left(\frac{dp}{dy}\right)^2$ term, we get:

$$\begin{aligned}&\frac{1}{3\pi^2}\left(-\frac{2Q^2m}{\rho^3R^2k_BT}\frac{dp}{dy} - \frac{2Q^2}{\rho^2R^3}\frac{dR}{dy}\right) = \frac{R^2}{\rho}\frac{dp}{dy}\left(-\frac{1}{2}+\frac{1}{7}\right) + gR^2\left(\frac{1}{2}-\frac{1}{7}\right)\\ &\qquad - \frac{10}{7}\nu U + \frac{12}{7}\frac{\nu u_s}{\sqrt{1+R'^2(y)}} + \frac{\nu}{2\pi}\left(\frac{2Qm^2}{k_B^2T^2\rho^3}\left(\frac{dp}{dy}\right)^2 - \frac{Q}{\rho^2}\frac{d^2p}{dy^2}\right)\\ &\Rightarrow -\frac{2}{3\pi^2}\frac{Q^2m}{\rho^3R^2k_BT}\frac{dp}{dy} - \frac{2}{3\pi^2}\frac{Q^2}{\rho^2R^3}\frac{dR}{dy} = -\frac{5}{14}\frac{R^2}{\rho}\frac{dp}{dy} + \frac{5}{14}gR^2 - \frac{10}{7}\nu U + \frac{12}{7}\frac{\nu u_s}{\sqrt{1+R'^2(y)}}\\ &\Rightarrow -\frac{2}{3\pi^2}\frac{Q^2m}{\rho^3R^2k_BT}\frac{dp}{dy} - \frac{2}{3\pi^2}\frac{Q^2}{\rho^2R^3}\frac{dR}{dy} = -\frac{5}{14}\frac{R^2}{\rho}\frac{dp}{dy} + \frac{5}{14}gR^2 - \frac{10}{7}\nu\left(\frac{210}{97\pi R^2}\frac{Q}{\rho} + \frac{2}{97}\frac{R^2}{\mu}\frac{dp}{dy}\right.\\ &\qquad \left. - \frac{2R^2\rho g}{97\mu} - \frac{102}{97}\frac{u_s}{\sqrt{1+R'(y)^2}}\right) + \frac{12}{7}\frac{\nu u_s}{\sqrt{1+R'^2(y)}} \qquad \text{using (4.15)}\\ &\qquad = -\frac{5}{14}\frac{R^2}{\rho}\frac{dp}{dy} - \frac{20}{679}\frac{R^2}{\rho}\frac{dp}{dy} - \frac{300\nu Q}{97\pi\rho R^2} + \frac{5}{14}gR^2 + \frac{20}{679}gR^2 + \frac{312}{97}\frac{\nu u_s}{\sqrt{1+R'^2(y)}}\\ &\qquad = -\frac{75}{194}\frac{R^2}{\rho}\frac{dp}{dy} + \frac{75}{194}gR^2 - \frac{300Q\nu}{97\pi\rho R^2} + \frac{312}{97}\frac{\nu u_s}{\sqrt{1+R'^2(y)}}\\ &\Rightarrow \frac{dp}{dy}\left(\frac{75}{194}\frac{R^2}{\rho} - \frac{2}{3\pi^2}\frac{Q^2m}{\rho^3R^2k_BT}\right) = \frac{75}{194}gR^2 + \frac{2}{3\pi^2}\frac{Q^2}{\rho^2R^3}\frac{dR}{dy} - \frac{300\nu Q}{97\pi\rho R^2} + \frac{312}{97}\frac{\nu u_s}{\sqrt{1+R'^2(y)}}\\ &\Rightarrow \frac{dp}{dy} = \frac{\frac{75}{194}gR^2 + \frac{2}{3\pi^2}\frac{Q^2}{\rho^2R^3}\frac{dR}{dy} - \frac{300\nu Q}{97\pi\rho R^2} + \frac{312}{97}\frac{\nu u_s}{\sqrt{1+R'^2(y)}}}{\left(\frac{75}{194}\frac{R^2}{\rho} - \frac{2}{3\pi^2}\frac{Q^2m}{\rho^3R^2k_BT}\right)}\end{aligned} \tag{B.9}$$

which is equation (4.18)

## B.3 Derivation of equation (4.19) and (4.20)

In this section, we provide the details of obtaining the velocity $u$ as given in equation (4.19). We have equation (4.13) and (4.14) as:

$$\begin{aligned}\frac{u}{U} &= \left(\frac{-\lambda+10-12E+\tilde{T}}{7}\right)\eta+\left(\frac{3\lambda+5-6E-3\tilde{T}}{7}\right)\eta^2 \\ &\quad+\left(\frac{-3\lambda-12+20E+3\tilde{T}}{7}\right)\eta^3+\left(\frac{\lambda+4-9E-\tilde{T}}{7}\right)\eta^4+E, \qquad \text{(B.10)}\\ \text{where}\quad &\lambda=\frac{dp}{dy}\frac{R^2}{\mu U},\\ &\tilde{T}=\frac{gR^2}{\nu U},\\ \text{and}\quad &E=\frac{u_s}{U\sqrt{1+R'(y)^2}},\end{aligned}$$

Substituting $\lambda$, $\tilde{T}$, $E$ and $\frac{dp}{dy}$ in equation (B.10) we get the following:

$$\begin{aligned}u=&\tfrac{1}{7}\left(-\tfrac{R^2}{\mu}\tfrac{dp}{dy}+10U-12\tfrac{u_s}{\sqrt{1+R'^2(y)}}+\tfrac{gR^2}{\nu}\right)\eta+\tfrac{1}{7}\left(\tfrac{3R^2}{\mu}\tfrac{dp}{dy}+5U-6\tfrac{u_s}{\sqrt{1+R'^2(y)}}-\tfrac{3gR^2}{\nu}\right)\eta^2\\ &+\tfrac{1}{7}\left(-\tfrac{3R^2}{\mu}\tfrac{dp}{dy}-12U+20\tfrac{u_s}{\sqrt{1+R'^2(y)}}+\tfrac{3gR^2}{\nu}\right)\eta^3+\tfrac{1}{7}\left(\tfrac{R^2}{\mu}\tfrac{dp}{dy}+4U-9\tfrac{u_s}{\sqrt{1+R'^2(y)}}-\tfrac{gR^2}{\nu}\right)\eta^4+\tfrac{u_s}{\sqrt{1+R'^2(y)}}\end{aligned} \qquad \text{(B.11)}$$

Now here are some details how to calculate the coefficients of $\eta$ in $u$:

$$\begin{aligned}\tfrac{R^2}{\mu}\tfrac{dp}{dy}&=\frac{\tfrac{R^2}{\mu}\left(\tfrac{75}{194}gR^2+\tfrac{2}{3}\tfrac{\pi^2\rho^2R^4\overline{U}^2}{\pi^2\rho^2R^3}\tfrac{dR}{dy}-\tfrac{300\nu\pi\rho R^2\overline{U}}{97\pi\rho R^2}+\tfrac{312}{97}\tfrac{\nu u_s}{\sqrt{1+R'^2(y)}}\right)}{\tfrac{75}{194}\tfrac{R^2}{\rho}\left(1-\tfrac{388\pi^2\rho^2R^2\overline{U}^2\rho m}{225\pi^2\rho^3R^2k_BT}\right)} \qquad \text{from (4.18)}\\ &=\frac{gR^2\rho}{\mu\left(1-\frac{388}{225}Ma^2\right)}+\frac{388}{225}\frac{R\rho\overline{U}^2}{\mu\left(1-\frac{388}{225}Ma^2\right)}\frac{dR}{dy}-\frac{8\overline{U}}{\left(1-\frac{388}{225}Ma^2\right)}+\frac{208}{25}\frac{1}{\left(1-\frac{388}{225}Ma^2\right)}\frac{u_s}{\sqrt{1+R'^2(y)}}\\ &=\frac{gR^2}{\nu\left(1-\frac{388}{225}Ma^2\right)}+\frac{388}{225}\frac{Re\overline{U}}{\left(1-\frac{388}{225}Ma^2\right)}\frac{dR}{dy}-\frac{8\overline{U}}{\left(1-\frac{388}{225}Ma^2\right)}+\frac{208}{25}\frac{1}{\left(1-\frac{388}{225}Ma^2\right)}\frac{u_s}{\sqrt{1+R'^2(y)}}\end{aligned} \qquad \text{(B.12)}$$

and

$$\begin{aligned}10U&=\tfrac{2100}{97\pi R^2}\tfrac{Q}{\rho}+\tfrac{20}{97}\tfrac{R^2}{\mu}\tfrac{dp}{dy}-\tfrac{20R^2g}{97\nu}-\tfrac{1020}{97}\tfrac{u_s}{\sqrt{1+R'(y)^2}} \qquad \text{from (4.15)}\\ &=\tfrac{2100}{97}\overline{U}+\tfrac{20}{97}\tfrac{R^2}{\mu}\tfrac{dp}{dy}-\tfrac{20R^2g}{97\nu}-\tfrac{1020}{97}\tfrac{u_s}{\sqrt{1+R'(y)^2}}\end{aligned} \qquad \text{(B.13)}$$

where we have used, $Q = \pi\rho R^2\overline{U}$, $Re = \frac{\overline{U}R}{\nu}$ for Reynolds number and $Ma = \frac{\overline{U}}{\sqrt{\frac{k_B T}{m}}}$ for the Mach number. To evaluate the coefficient of $\eta$ in equation (B.11), we substituted (B.12) and (B.13) in the following way:

$$
\begin{aligned}
&\tfrac{1}{7}\left( -\tfrac{R^2}{\mu}\tfrac{dp}{dy} + 10U - 12\tfrac{u_s}{\sqrt{1+R'^2(y)}} + \tfrac{gR^2}{\nu}\right)\\
&= \tfrac{1}{7}\Bigg( -\tfrac{gR^2}{\nu\left(1-\frac{388}{225}Ma^2\right)} - \tfrac{388}{225}\tfrac{Re\overline{U}}{\left(1-\frac{388}{225}Ma^2\right)}\tfrac{dR}{dy} + \tfrac{8\overline{U}}{\left(1-\frac{388}{225}Ma^2\right)} - \tfrac{208}{25}\tfrac{1}{\left(1-\frac{388}{225}Ma^2\right)}\tfrac{u_s}{\sqrt{1+R'^2(y)}}\\
&+\tfrac{2100}{97}\overline{U} + \tfrac{20}{97}\left(\tfrac{gR^2}{\nu\left(1-\frac{388}{225}Ma^2\right)} + \tfrac{388}{225}\tfrac{Re\overline{U}}{\left(1-\frac{388}{225}Ma^2\right)}\tfrac{dR}{dy} - \tfrac{8\overline{U}}{\left(1-\frac{388}{225}Ma^2\right)} + \tfrac{208}{25}\tfrac{1}{\left(1-\frac{388}{225}Ma^2\right)}\tfrac{u_s}{\sqrt{1+R'^2(y)}}\right)\\
&-\tfrac{20R^2g}{97\nu} - \tfrac{1020}{97}\tfrac{u_s}{\sqrt{1+R'(y)^2}} - 12\tfrac{u_s}{\sqrt{1+R'^2(y)}} + \tfrac{gR^2}{\nu}\Bigg)\\
&= -\tfrac{44}{225}\tfrac{gR^2Ma^2}{\nu\left(1-\frac{388}{225}Ma^2\right)} - \tfrac{44}{225}\tfrac{\overline{U}Re}{\left(1-\frac{388}{225}Ma^2\right)}\tfrac{dR}{dy} + \tfrac{\overline{U}}{\left(1-\frac{388}{225}Ma^2\right)}\left(4-\tfrac{16}{3}Ma^2\right)\\
&-\tfrac{u_s}{\sqrt{1+R'^2(y)}\left(1-\frac{388}{225}Ma^2\right)}\left(\tfrac{104}{25}-\tfrac{416}{75}Ma^2\right)
\end{aligned}
\tag{B.14}
$$

By using the same procedure we got the coefficient of $\eta^2$ as:

$$
\begin{aligned}
&\tfrac{1}{7}\left(\tfrac{3R^2}{\mu}\tfrac{dp}{dy} + 5U - 6\tfrac{u_s}{\sqrt{1+R'^2(y)}} - \tfrac{3gR^2}{\nu}\right)\\
&= \tfrac{172}{225}\tfrac{gR^2Ma^2}{\nu\left(1-\frac{388}{225}Ma^2\right)} + \tfrac{172}{225}\tfrac{\overline{U}Re}{\left(1-\frac{388}{225}Ma^2\right)}\tfrac{dR}{dy} + \tfrac{\overline{U}}{\left(1-\frac{388}{225}Ma^2\right)}\left(-2-\tfrac{8}{3}Ma^2\right)\\
&+\tfrac{u_s}{\sqrt{1+R'^2(y)}\left(1-\frac{388}{225}Ma^2\right)}\left(\tfrac{52}{25}+\tfrac{208}{75}Ma^2\right),
\end{aligned}
\tag{B.15}
$$

coefficient of $\eta^3$ as:

$$
\begin{aligned}
&\tfrac{1}{7}\left(\tfrac{-3R^2}{\mu}\tfrac{dp}{dy} - 12U + 20\tfrac{u_s}{\sqrt{1+R'^2(y)}} + \tfrac{3gR^2}{\nu}\right)\\
&= -\tfrac{4}{5}\tfrac{gR^2Ma^2}{\nu\left(1-\frac{388}{225}Ma^2\right)} - \tfrac{4}{5}\tfrac{\overline{U}Re}{\left(1-\frac{388}{225}Ma^2\right)}\tfrac{dR}{dy} + \tfrac{\overline{U}}{\left(1-\frac{388}{225}Ma^2\right)}\left(\tfrac{32}{5}Ma^2\right)\\
&+\tfrac{u_s}{\sqrt{1+R'^2(y)}\left(1-\frac{388}{225}Ma^2\right)}\left(\tfrac{4}{5}-\tfrac{1808}{225}Ma^2\right),
\end{aligned}
\tag{B.16}
$$

coefficient of $\eta^4$ as:

$$\begin{aligned}
&\tfrac{1}{7}\left(\tfrac{R^2}{\mu}\tfrac{dp}{dy}+4U-9\tfrac{u_s}{\sqrt{1+R'^2(y)}}-\tfrac{gR^2}{\nu}\right)\\
&=\tfrac{4}{15}\tfrac{gR^2Ma^2}{\nu\left(1-\frac{388}{225}Ma^2\right)}+\tfrac{4}{15}\tfrac{\overline{U}Re}{\left(1-\frac{388}{225}Ma^2\right)}\tfrac{dR}{dy}+\tfrac{\overline{U}}{\left(1-\frac{388}{225}Ma^2\right)}\big(-\tfrac{32}{15}Ma^2\big)\\
&+\tfrac{u_s}{\sqrt{1+R'^2(y)}\left(1-\frac{388}{225}Ma^2\right)}\Big(-\tfrac{3}{5}+\tfrac{244}{75}Ma^2\Big),
\end{aligned}\tag{B.17}$$

Substituting all those (B.14), (B.15), (B.16) and (B.17) in equation (B.11) and dividing by $\overline{U}$ gives:

$$\begin{aligned}
&\tfrac{u}{\overline{U}}\\
&=\tfrac{gR^2Ma^2}{\nu\overline{U}\left(1-\frac{388}{225}Ma^2\right)}\left(-\tfrac{44}{225}\eta+\tfrac{172}{225}\eta^2-\tfrac{4}{5}\eta^3+\tfrac{4}{15}\eta^4\right)\\
&+\tfrac{Re}{\left(1-\frac{388}{225}Ma^2\right)}\tfrac{dR}{dy}\left(-\tfrac{44}{225}\eta+\tfrac{172}{225}\eta^2-\tfrac{4}{5}\eta^3+\tfrac{4}{15}\eta^4\right)\\
&+\tfrac{1}{\left(1-\frac{388}{225}Ma^2\right)}\left((4-\tfrac{16}{3}Ma^2)\eta+\big(-2-\tfrac{8}{3}Ma^2\big)\eta^2+\tfrac{32}{5}Ma^2\eta^3-\tfrac{32}{15}Ma^2\eta^4\right)\\
&+\tfrac{u_s}{\overline{U}\sqrt{1+R'^2(y)}\left(1-\frac{388}{225}Ma^2\right)}\left(-\tfrac{104}{25}\eta+\tfrac{52}{25}\eta^2+\tfrac{4}{5}\eta^3-\tfrac{3}{5}\eta^4+1+\Big(\tfrac{416}{75}\eta+\tfrac{208}{75}\eta^2-\tfrac{1808}{225}\eta^3+\tfrac{244}{75}\eta^4-\tfrac{388}{225}\Big)Ma^2\right),
\end{aligned}\tag{B.18}$$

which is (4.19) as desired.

Now to get the velocity scaled by the average upstream velocity, $\overline{U}_0$, we have used the following relation:

$$\begin{aligned}
&\tfrac{u}{\overline{U}_0}=\big(\tfrac{u}{\overline{U}}\big)\big(\tfrac{\overline{U}}{\overline{U}_0}\big)\\
&=\Big(\tfrac{\left(\frac{R_0}{R}\right)^2\left(\frac{\rho_0}{\rho}\right)}{\left(1-\frac{388}{225}Ma^2\right)}\Big)\Bigg[Ma^2\big(\tfrac{R_0g}{\overline{U}_0^2}\big)Re_0\big(\tfrac{R}{R_0}\big)^4\big(\tfrac{\rho}{\rho_0}\big)\big(\tfrac{\nu_0}{\nu}\big)\left(-\tfrac{44}{225}\eta+\tfrac{172}{225}\eta^2-\tfrac{4}{5}\eta^3+\tfrac{4}{15}\eta^4\right)\\
&+Re_0\big(\tfrac{\rho_0}{\rho}\big)\big(\tfrac{R_0}{R}\big)\big(\tfrac{\nu_0}{\nu}\big)\big(\tfrac{dR}{dy}\big)\left(-\tfrac{44}{225}\eta+\tfrac{172}{225}\eta^2-\tfrac{4}{5}\eta^3+\tfrac{4}{15}\eta^4\right)\\
&+\left((4-\tfrac{16}{3}Ma^2)\eta+\big(-2-\tfrac{8}{3}Ma^2\big)\eta^2+\tfrac{32}{5}Ma^2\eta^3-\tfrac{32}{15}Ma^2\eta^4\right)\\
&+\Big(\tfrac{u_s}{\sqrt{1+R'^2(y)}}\big(\tfrac{R}{R_0}\big)^2\tfrac{\rho}{\rho_0}\tfrac{1}{\overline{U}_0}\Big)\left(-\tfrac{104}{25}\eta+\tfrac{52}{25}\eta^2+\tfrac{4}{5}\eta^3-\tfrac{3}{5}\eta^4+1+\Big(\tfrac{416}{75}\eta+\tfrac{208}{75}\eta^2-\tfrac{1808}{225}\eta^3+\tfrac{244}{75}\eta^4-\tfrac{388}{225}\Big)Ma^2\right)\Bigg],
\end{aligned}\tag{B.19}$$

Now for $\eta = 1$ we have the expression as in the following form:

$$\begin{aligned}
\tfrac{u}{U_0} &= \tfrac{u}{2\overline{U}_0} \\
&= \tfrac{1}{2}\big(\tfrac{u}{\overline{U}}\big)\big(\tfrac{\overline{U}}{\overline{U}_0}\big) \\
&= \tfrac{(\frac{R_0}{R})^2(\frac{\rho_0}{\rho})}{2\big(1-\frac{388}{225}Ma^2\big)}\Bigg[\tfrac{8}{225}Ma^2\Big(\tfrac{R_0 g}{\overline{U}_0^2}\Big)Re_0\Big(\tfrac{R}{R_0}\Big)^4\Big(\tfrac{\rho}{\rho_0}\Big)\Big(\tfrac{\nu_0}{\nu}\Big) \\
&+ \tfrac{8}{225}Re_0\Big(\tfrac{\rho_0}{\rho}\Big)\Big(\tfrac{R_0}{R}\Big)\Big(\tfrac{\nu_0}{\nu}\Big)\tfrac{dR}{dy} + \Big(2 - \tfrac{56}{15}Ma^2\Big) \\
&+ \tfrac{u_s}{\sqrt{1+R'^2(y)}}\big(\tfrac{R}{R_0}\big)^2\tfrac{\rho}{\rho_0}\tfrac{1}{\overline{U}_0}\Big(-\tfrac{22}{25} + \tfrac{136}{75}Ma^2\Big)\Bigg],
\end{aligned} \tag{B.20}$$

which is (4.20) as desired.

# References


[1] E. Allahyarov and G. Gompper. Mesoscopic solvent simulations: Multiparticle-collision dynamics of three-dimensional flow. *Phys. Rev. E*, 66:036702–1–9, 2002.

[2] S. K. Bedkihal. Simulations of steady flows through cylindrical geometries with and without local constrictions by multiparticle collision dynamics. *Masters Thesis, Biomedical Physics, Ryerson University.*, 2010.

[3] G.A. Bird. *Molecular gas dynamics and the direct simulation of gas flows.* Oxford University Press, 1994.

[4] V. Chikkadi and M. Alam. Slip velocity and stresses in granular poiseuille flow via event-driven simulation. *Phys. Rev. E*, 80:021303–1–16, 2009.

[5] J.R. Darias, M. Quiroga, E. Medina, P.J. Colmenares, and R. Paredes V. Simulation of suspensions in constricted geometries by dissipative particle dynamics. *Molec. Sim.*, 29:443–449, 2003.

[6] Biswas Devajoyoti. *Blood flow models: A Compressible Study.* Mittal, 2004.

[7] M. T. Downton and H. Stark. Simulation of model microswimmer. *Journal of Physics, Condensed Matter.*, 21:204101, 2009.

[8] D. J. Evans and G. P. Morris. Shear thickening and turbulence in simple fluids. *Physical Review Letters*, 56:2172–2175, 1986.

[9] J. H. Forrester. Flow through a converging-diverging tube and it's implications in occlusive vascular disease. *Ph. D. Thesis Ames, Iowa, Library, Iowa State University.*, 1968.

[10] J. H. Forrester and D. F. Young. Flow through a converging-diverging tube and it's implications in occlusive vascular disease-I: Theoretical development. *J.Biomechanics.*, 3:297–385, 1970.

[11] J. H. Forrester and D. F. Young. Flow through a converging-diverging tube and it's implications in occlusive vascular disease-II: Theoretical and experimental results and their implications. *J.Biomechanics.*, 3:307–310, 1970.

[12] G. Gompper, T. Ihle, D.M. Kroll, and R.G. Winkler. Multi-particle collision dynamics: A particle-based mesoscale simulation approach to the hydrodynamics of complex fluids. *Adv. Polym. Sci.*, 221:1–87, 2009.

[13] D. Hershey and S. J. Cho. Blood flow in rigid tubes, thickness and slip velocity of plasma film at the wall. *Journal of Applied Physiology.*, 21:27–32, 1966.

[14] P. J. Hoogerbrugge and J. M. Koelman. Simulating microscopic hydrodynamic phenomena with dissipative particle dynamics. *Europhysics Letters*, 19:155–160, 1992.

[15] A. C. L. Hunt, W. A Timlake, W. P. Barnard, and Varley E. A theory of fluid flow in compliant tubes. *Biophys J.*, 6:717–724, 1996.

[16] T. Ihle and D.M. Kroll. Stochastic rotation dynamics: A Galilean-invariant mesoscopic model for fluid flow. *Phys. Rev. E*, 63:020201–1–4, 2001.

[17] T. Ihle and D.M. Kroll. Stochastic rotation dynamics, formalism -I, galilean-invariance, and green-kubo relations. *Phys. Rev. E*, 67:066705, 2003.

[18] M. J. Kang, H-S. Ji, and S.J. Lee. In-vitro study on haemodiluted blood flow in a sinusoidal microstenosis. *Proc. IMechE Part H: J. Engineering in Medicine*, 224:17–25, 2009.

[19] R. Kapral. Multiparticle collision dynamics: Simulation of complex systems on mesoscales. *Adv. Chem. Phys.*, 140:89–146, 2008.

[20] A. Lamura and G. Gompper. Numerical study of the flow around a cylinder using multi-particle collision dynamics. *Eur. Phys. J. E*, 9:477–485, 2002.

[21] J. S. Lee. Numerical study of fluid flow through double bell-shaped constrictions in a tube. *International Journal of Numerical Methods for Heat & Fluid Flow*, 12:258–289, 2002.

[22] A. Malevanets and R. Kapral. Mesoscopic model for solvent dynamics. *J. Chem. Phys.*, 110:8605–8613, 1999.

[23] A. Malevanets and R. Kapral. Mesoscopic multiparticle collision model for fluid flows and molecular dynamics. *Lect. Notes. Physics, Springer Verlarg Berlin Heidelberg.*, 640:116–149, 2000.

[24] D. K. Mandal, N. K. Manna, and S. Chakrabarti. Influence of primary stenosis on secondary one and vice versa in case of double stenosis. *Journal of Applied Fluid Mechanics.*, 4:31–42, 2011.

[25] A. Medhavi. On macroscopic two-phase arterial blood flow through an overlapping stenosis. *e -Journal of Science & Technology (e-JST).*, 2011.

[26] J.C. Misra and G.C. Shit. Role of slip velocity in blood flow through stenosed arteries: A non-Newtonian model. *J. Mech. Med. Biol.*, 7:337–353, 2007.

[27] A. Nakano, Y. Sugii, M. Minamiyama, J. Seki, and H. Miimi. Velocity profiles of pulsatile blood flow in arterioles with bifurcation and confluence in rat mesentary measured by particle image velocimetry. *JSME International Journal - Mechanical Systems Machine Elements and Manufacturing*, 48:444–452, 2005.

[28] H. Noguchi and G. Gompper. Transport coefficients of off-lattice mesoscale-hydrodynamics simulation techniques. *Phys. Rev. E*, 78:016706–1–12, 2008.

[29] H. Noguchi, N. Kikuchi, and G. Gompper. Particle based mesoscale hydrodynamic techniques. *European Physics Letters*, 78:016706, 2007.

[30] Y. Nubar. Blood flow, slip, and viscometry. *Biophys. J.*, 11:252–264, 1971.

[31] J.T. Padding and A.A. Louis. Hydrodynamic interactions and Brownian forces in colloidal suspensions: Coarse-graining over time and length scales. *Phys. Rev. E*, 74:031402–1–29, 2006.

[32] N. Padmanabhan. Mathematical model of arterial stenosis. *Med. & Biol. Eng. & Computer*, 18:281–226, 1980.

[33] C. Picart, J.M. Piau, H. Gilliard, and P. Carpentier. Human blood shear yield stress and hematocrit dependence. *J. Rheology*, 42:1–12, 1998.

[34] R.N. Pralhad and D.H. Schultz. Modeling of arterial stenosis and its applications to blood diseases. *Math. Biosciences*, 190:203–220, 2004.

[35] D.A.P. Reid, H. Hildenbrandt, J.T. Padding, and C.K. Hemelrijk. Flow around fishlike shapes studies using multiparticle collision dynamics. *Phys. Rev. E*, 79:046313–1–7, 2009.

[36] H. Schlichting. *Boundary Layer Theory, 6th Edition*, volume 45. McGraw-Hill, New York, 1968.

[37] J. S. Stroud and S. A. Berger. Numerical analysis of flow through a severely stenotic carotid artery bifurcation. *Journal of Biomechanical Engineering.*, 124:9–20, 2002.

[38] M.W. Tysanner and A.L. Garcia. Non-equilibrium behaviour of equilibrium reservoirs in molecular simulations. *Int. J. Numer. Meth. Fluids*, 48:1337–1349, 2005.

[39] S.S. Varghese, S.H. Frankel, and P.F. Fischer. Direct numerical simulation of stenotic flows. part 1. steady flow. *J. Fluid Mech.*, 582:253–280, 2007.

[40] F. M. White. *Fluid Mechanics/ Frank M. White.* McGraw-Hill, 2003.

[41] J.K. Whitmer and E. Luijten. Fluid-solid boundary conditions for multiparticle collision dynamics. *J. Phys.: Condens. Matter*, 22:104106–1–14, 2010.

[42] D. F. Young. Effect of a time-dependent stenosis on flow through a tube. *J. Engng Ind*, 90:248–254, 1968.

[43] J. G. Zhou. Axisymmetric lattice Boltzmann method. *Phys. Rev. E*, 78:036701–1–7, 2008.